RSC Advances

PAPER

View Article Online
View Journal | View Issue

Cite this: *RSC Adv.*, 2023, **13**, 27801

Synthesis, biological evaluation and computer-aided discovery of new thiazolidine-2,4-dione derivatives as potential antitumor VEGFR-2 inhibitors†

Hazem Elkady, *[a] Osama A. El-Dardir,[b] Alaa Elwan, [a] Mohammed S. Taghour,[a] Hazem A. Mahdy, [a] Mohammed A. Dahab, [a] Eslam B. Elkaeed, [c] Bshra A. Alsfouk,[d] Ibrahim M. Ibrahim,[e] Dalal Z. Husein,[f] Elsayed E. Hafez,[g] Amira M. G. Darwish, [hi] Ahmed M. Metwaly [j] and Ibrahim H. Eissa *[a]

In this study, novel VEGFR-2-targeting thiazolidine-2,4-dione derivatives with potential anticancer properties were designed and synthesized. The ability of the designed derivatives to inhibit VEGFR-2 and stop the growth of three different cancer cell types (HT-29, A-549, and HCT-116) was examined *in vitro*. The IC_{50} value of compound **15**, 0.081 μM, demonstrated the best anti-VEGFR-2 potency. Additionally, compound **15** showed remarkable anti-proliferative activities against the tested cancer cell lines, with IC_{50} values ranging from 13.56 to 17.8 μM. Additional flow cytometric investigations showed that compound **15** increased apoptosis in HT-29 cancer cells (from 3.1% to 31.4%) arresting their growth in the S phase. Furthermore, compound **15**'s apoptosis induction in the same cell line was confirmed by increasing the levels of BAX (4.8-fold) and decreasing Bcl-2 (2.8-fold). Also, compound **15** noticeably increased caspase-8 and caspase-9 levels by 1.7 and 3.2-fold, respectively. Computational methods were used to perform molecular analysis of the VEGFR-2-**15** complex. Molecular dynamics simulations and molecular docking were utilized to analyze the complex's kinetic and structural characteristics. Protein–ligand interaction profiler analysis (PLIP) determined the 3D interactions and binding conformation of the VEGFR-2-**15** complex. DFT analyses also provided insights into the 3D geometry, reactivity, and electronic characteristics of compound **15**. Computational ADMET and toxicity experiments were conducted to determine the potential of the synthesized compounds for therapeutic development. The study's findings suggest that compound **15** might be an effective anticancer lead compound and could guide future attempts to develop new drugs.

Received 21st August 2023
Accepted 11th September 2023

DOI: 10.1039/d3ra05689a

rsc.li/rsc-advances

1. Introduction

The task of discovering effective treatments for cancer is a complex and challenging process that requires a comprehensive understanding of the intricate biological mechanisms underlying the disease's development and progression.[1] Consequently, chemotherapy remains an active area of research to develop novel therapeutics that can enhance patient outcomes and ultimately reduce the incidence of cancer.[2]

Receptor tyrosine kinases (RTKs) constitute a crucial class of protein kinases that mediate both inter- and intracellular communication through signal transduction.[3,4] These proteins

[a]*Pharmaceutical Medicinal Chemistry & Drug Design Department, Faculty of Pharmacy (Boys), Al-Azhar University, Cairo, 11884, Egypt. E-mail: Hazemelkady@azhar.edu.eg; alaaelwan34@azhar.edu.eg; mohammad1533.el@azhar.edu.eg; hazem_hady2001@azhar.edu.eg; mohammeddahab@azhar.edu.eg; Ibrahimeissa@azhar.edu.eg*

[b]*Undergraduate Student, Faculty of Pharmacy, Al-Azhar University, Cairo 11884, Egypt. E-mail: Osamaeldardiri.2.stu.1@azhar.edu.eg*

[c]*Department of Pharmaceutical Sciences, College of Pharmacy, AlMaarefa University, Riyadh 13713, Saudi Arabia. E-mail: ikaeed@mcst.edu.sa*

[d]*Department of Pharmaceutical Sciences, College of Pharmacy, Princess Nourah bint Abdulrahman University, P.O. Box 84428, Riyadh 11671, Saudi Arabia. E-mail: baalsfouk@pnu.edu.sa*

[e]*Biophysics Department, Faculty of Science, Cairo University, Giza 12613, Egypt. E-mail: ibrahim_mohamed@cu.edu.eg*

[f]*Chemistry Department, Faculty of Science, New Valley University, El-Kharja 72511, Egypt. E-mail: dalal_husein@sci.nvu.edu.eg*

[g]*Plant Protection and Biomolecular Diagnosis, ALCRI, City of scientific research and technological applications, New Borg El-Arab City, Alexandria, 21934, Egypt. E-mail: elsayed_hafez@yahoo.com*

[h]*Food Industry Technology Program, Faculty of Industrial and Energy Technology, Borg Al Arab Technological University, Alexandria, Egypt*

[i]*Food Technology Department, Arid Lands Cultivation Research Institute, City of Scientific Research and Technological Applications (SRTA-City), Alexandria 21934, Egypt. E-mail: amiragdarwish@yahoo.com*

[j]*Pharmacognosy and Medicinal Plants Department, Faculty of Pharmacy (Boys), Al-Azhar University, Cairo 11884, Egypt*

† Electronic supplementary information (ESI) available. See DOI: https://doi.org/10.1039/d3ra05689a

play a pivotal role in regulating essential cellular processes, such as cell growth, differentiation, metabolism, survival, and proliferation.[5] One prominent member of the RTK family is the vascular endothelial growth factor receptor-2 (VEGFR-2), which directly regulates endothelial cell migration and proliferation.[6] In cancer cells, VEGFR-2 has been identified as a prominent positive regulator of cancer progression, including proliferation, migration, and angiogenesis.[7] In addition, a multitude of cancer types have been found to demonstrate an upregulation of VEGFR-2 expression.[8] Accordingly, due to its central role in angiogenesis regulation, VEGFR-2 is considered a vital target for suppressing cancer growth and metastasis.[9]

Over the past two decades, computational chemistry has emerged as a potent tool for analyzing the physical, chemical, and molecular properties of compounds, enabling researchers to gain valuable insights into the molecular characteristics of compounds and their interactions with different proteins.[10] With the help of computational chemistry, researchers can precisely evaluate the efficacy of drug candidates and design new molecules with desired properties, potentially accelerating the drug development process and enhancing the quality of treatments. This has significant implications for the field of medicinal chemistry, where computational chemistry is rapidly gaining popularity as an effective approach for optimizing drug discovery and design.[11,12]

Utilizing computational chemistry, our laboratory discovered a multitude of potential anti-cancer agents that exhibit VEGFR-2 inhibitory activity. These agents are derived from diverse chemical classes and derivatives, including nicotinamides,[13,14] thiazolidines,[15,16] naphthalenes,[17] pyridines,[18] quinolines[19] indoles,[20] and isatins.[21]

1.2. The rationale of molecular design

The VEGFR-2 inhibitors have four pharmacophoric features required for efficient binding in the active site of VEGFR-2. Each feature should be oriented into a specific sub-pocket in the active site. In detail, the first feature is a heteroaromatic system that should be oriented into the hinge region, forming an essential hydrogen bonding (H-bonding) interaction with the amino acid Cys917.[22] The second feature is the linker moiety, which should be positioned within the gatekeeper region. The linker moiety provides a suitable length for the designed VEGFR-2 inhibitors, enabling the other groups to be oriented into the specific sub-pocket.[23] The third feature is the pharmacophore structure, which should be aligned with the DFG domain, forming at least two H-bonding interactions with the amino acids Glu883 and Asp1044. The pharmacophore moiety should possess at least one H-bond donor and one H-bond acceptor group to achieve the maximal fitting with the receptor.[24] The fourth feature is the hydrophobic tail, which should be oriented into the allosteric binding pocket to form hydrophobic interactions.[25–27]

VEGFR-2 inhibitors can be classified into many categories according to the chemical structures of the heteroaromatic system and the pharmacophore moieties, as shown in Fig. 1. Sorafenib **I** is an example of the first class. It comprises a pyridine moiety as a heterocyclic system and a urea moiety as a pharmacophore.[28,29] Sunitinib **II** is an example of the second class of VEGFR-2 inhibitors. It incorporates an indoline moiety as a heterocyclic system and an amide group as a pharmacophore.[30,31] Lenvatinib **III** is a third-class member constitutes a quinoline moiety as a heterocyclic system and a urea group as a pharmacophore.[32–34]

Recently, our research group introduced some modified benzoxazole-based VEGFR-2 inhibitors and apoptosis inducers. For instance, compound **IV** exerted good VEGFR-2 inhibitory activity with excellent cytotoxic effects. It showed a significant apoptotic effect and arrested the HepG2 cells at the pre-G1 phase. In addition, it exerted a significant inhibition for TNF-α and IL-6.[35]

In this work, as part of our ongoing research on VEGFR-2 inhibitors, a new series of 5-benzylidenethiazolidine-2,4-dione was designed as modified analogs of compound **IV**, containing the four features of VEGFR-2 inhibitors. In detail, the benzoxazole moiety of compound **IV** was replaced by a 5-benzylidenethiazolidine-2,4-dione moiety as a heterocyclic system. Shortening of the 2-sulfanyl-*N*-phenylacetamide linker of compound **IV** was achieved to be phenyl acetamide linker in the new compounds. The pharmacophore (amide) moiety of compound **IV** was kept in the new compounds. Finally, the 4-nitrophenyl moiety of compound **IV** was replaced by a cyclopentyl and or different substituted phenyl rings as a terminal hydrophobic tail (Fig. 2).

2. Experimental

2.1. Chemistry

All reagents, solvents, and fine chemicals were obtained from Sigma-Aldrich (Poole, Dorset, UK) and EL NASR company for intermediate chemicals (Cairo, Egypt). The purity of the purchased materials was more than 98%. Compounds **3**, **5a–c**, **6a–c**, and **11a–e** were synthesized as previously reported.[21,36–40]

2.1.1. General procedure for the synthesis of target compounds 12–17. Equimolar amounts of the appropriate potassium salts **6a–c** (0.001 mol) were heated with appropriate intermediates **11a–e** (0.001 mol) for 6 h in dry DMF (10 mL) in the presence of KI (0.001 mol). The reaction mixture was stirred for 30 minutes after being poured into 200 mL of ice water. The resultant solids were filtered, washed with water, dried, and crystallized from ethanol to obtain the relevant target compounds **12–17**.

*2.1.1.1. 4-(2-(5-Benzylidene-2,4-dioxothiazolidin-3-yl)acetamido)-N-cyclopentylbenzamide **12**.*

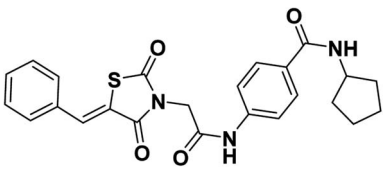

Colorless crystals (yield, 75%); mp = 210–212 °C; IR (KBr) ν cm^{-1}: 3258 (NH), 1745, 1695, 1668 (C=O); ^{1}H NMR (400 MHz, DMSO-d_6) δ 10.63 (s, 1H, NH), 8.18 (d, J = 7.3 Hz, 1H, NH), 8.06 (s, 1H, –C=CH), 7.85 (dd, J = 8.4, 3.4 Hz, 3H, Ar–H), 7.62 (t, J = 9.3 Hz, 4H, Ar–H), 7.45 (t, J = 7.6 Hz, 2H, Ar–H), 4.58

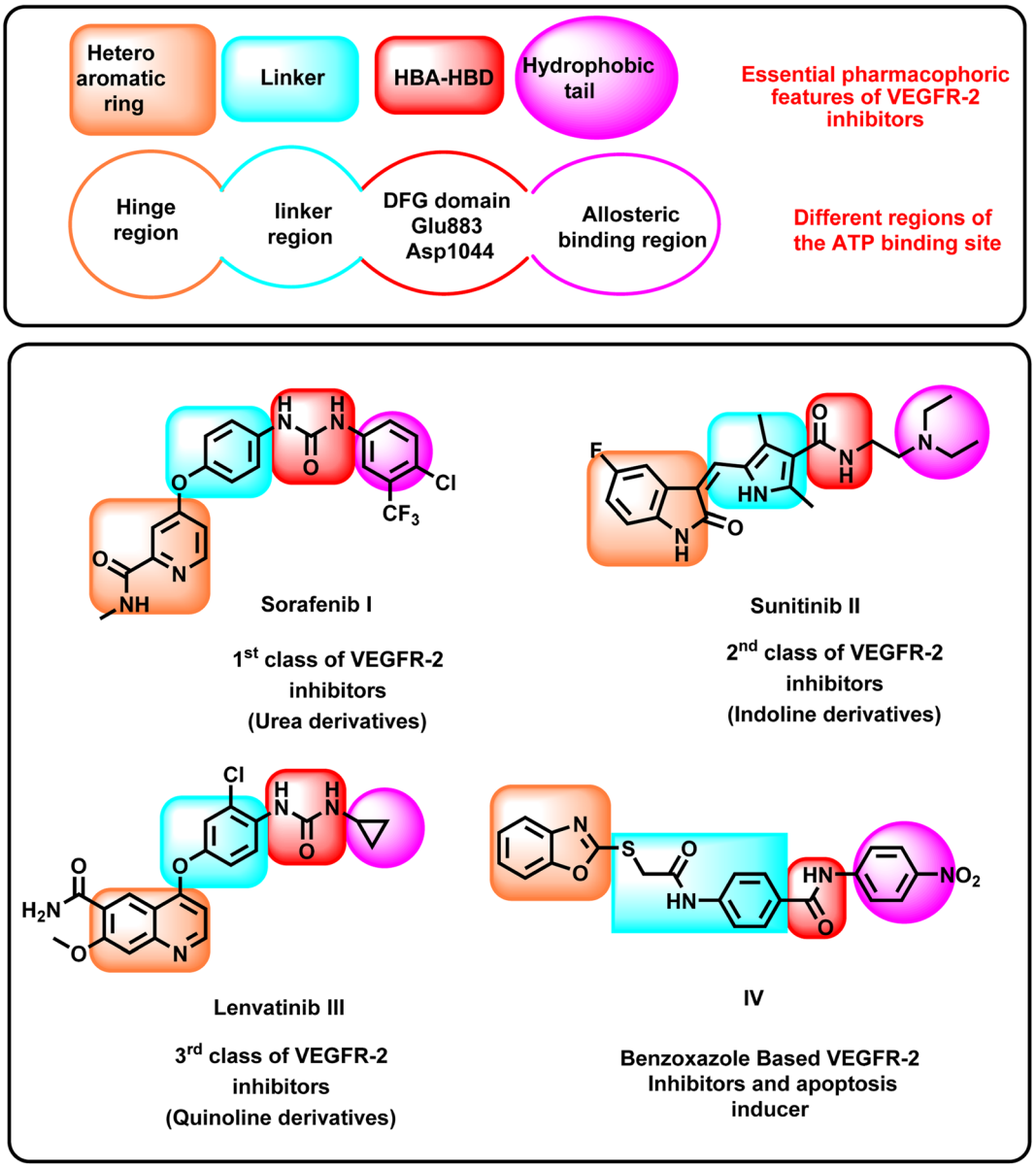

Fig. 1 Some reported VEGFR-2 inhibitors showing their essential pharmacophoric features.

(s, 2H, CH_2), 4.22 (h, J = 7.2 Hz, 1H, CH of cyclopentyl), 1.88 (dt, J = 11.1, 6.3 Hz, 2H, 2CH of cyclopentyl), 1.68 (d, J = 12.4 Hz, 2H, 2CH of cyclopentyl), 1.60–1.44 (m, 4H, 4CH of cyclopentyl); ^{13}C NMR (101 MHz, DMSO-d_6) δ ppm: 167.36, 165.72, 165.32, 164.53, 141.11, 134.15, 133.10, 132.82, 131.97, 130.34, 129.65, 129.20, 128.75, 125.78, 125.20, 118.78, 51.38, 44.68, 32.78, 32.62, 24.11; anal. calcd. for $C_{24}H_{23}N_3O_4S$ (449.53): C, 64.13; H, 5.16; N, 9.35. Found: C, 64.29; H, 5.30; N, 9.54%; ESI-MS (m/z): 448.2826 $[M-1]^-$, 449.2831 $[M]^-$; HPLC purity 95.21%.

2.1.1.2. 4-(2-(5-Benzylidene-2,4-dioxothiazolidin-3-yl)acetamido)-N-(4-fluorophenyl) benzamide ***13****.*

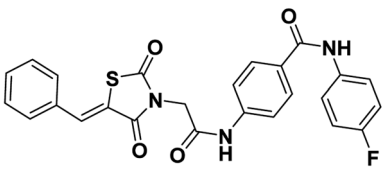

Colorless crystals (yield, 78%); mp = 225–227 °C; IR (KBr) ν cm^{-1}: 3258 (NH), 1745, 1695, 1668 (C=O); ^{1}H NMR (400 MHz, DMSO-d_6) δ 10.71 (s, 1H, NH), 10.21 (s, 1H, NH), 8.03 (s, 1H, –C=CH), 7.98 (d, J = 8 Hz, 2H, Ar–H), 7.79 (dd, J = 8.8, 5.0 Hz, 2H, Ar–H), 7.71 (m, 4H, Ar–H), 7.58 (m, 3H, Ar–H), 7.20 (t, J = 8.7 Hz, 2H, Ar–H), 4.59 (s, 2H, CH_2); ^{13}C NMR (101 MHz, DMSO-

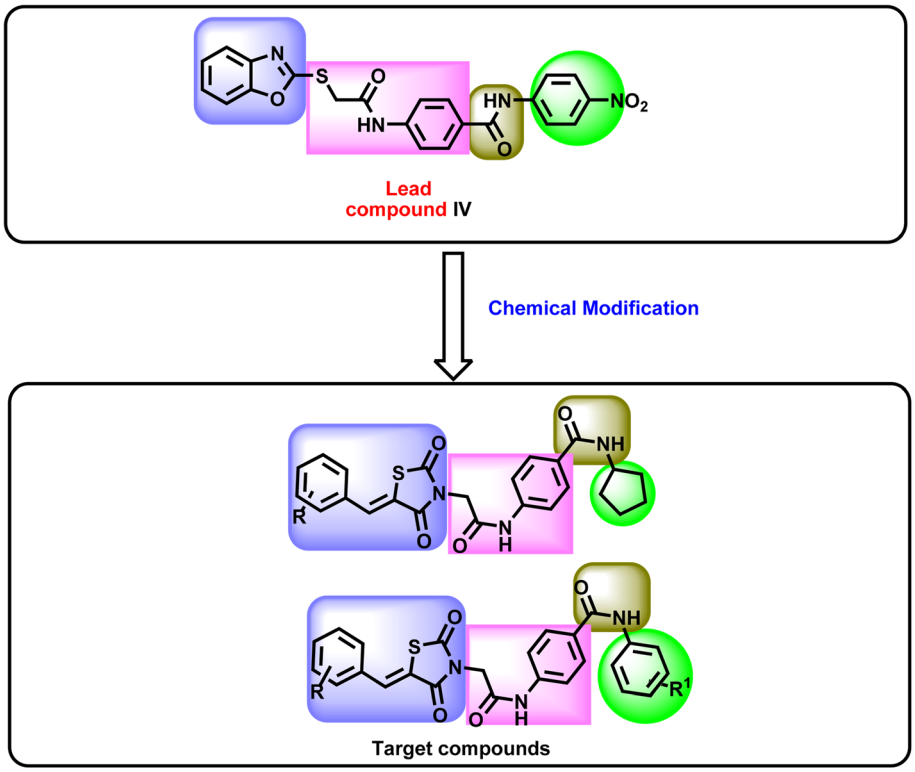

Fig. 2 Schematic summary for the rationale of molecular design.

d_6) δ ppm: 167.61, 165.77, 165.17, 164.78, 141.78, 136.08, 134.20, 133.34, 131.34, 130.71, 130.06, 129.93, 129.22, 122.65, 122.58, 121.43, 118.95, 115.73, 115.51, 44.64; anal. calcd. for $C_{25}H_{18}FN_3O_4S$ (475.49): C, 63.15; H, 3.82; N, 8.84. Found: C, 63.45; H, 4.05; N, 8.72%; ESI-MS (m/z): 474.1915 $[M-1]^+$, 475.2205 $[M]^+$; HPLC purity 100.00%.

2.1.1.3. 4-(2-(5-(2-Bromobenzylidene)-2,4-dioxothiazolidin-3-yl)acetamido)-N-(4-fluorophenyl) benzamide ***14****.*

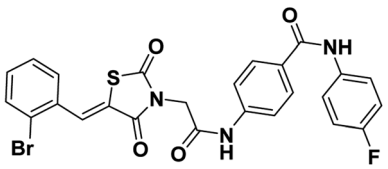

Colorless crystals (yield, 72%); mp = 220–222 °C; IR (KBr) ν cm^{-1}: 3268 (NH), 1752, 1697, 1670 (C=O); ^{1}H NMR (400 MHz, DMSO-d_6) δ 10.73 (s, 1H, NH), 10.22 (s, 1H, NH), 8.07 (s, 1H, –C=CH), 7.99 (d, J = 8.3 Hz, 2H, Ar–H), 7.81 (q, J = 6.7, 5.2 Hz, 3H, Ar–H), 7.74 (d, J = 8.3 Hz, 2H, Ar–H), 7.67–7.53 (m, 2H, Ar–H), 7.44 (t, J = 6.7 Hz, 1H, Ar–H), 7.19 (t, J = 8.7 Hz, 2H, Ar–H), 4.61 (s, 2H, CH_2); ^{13}C NMR (101 MHz, DMSO-d_6) δ ppm: 167.38, 165.33, 165.17, 164.68, 141.76, 136.08, 136.05, 134.14, 133.08, 132.97, 132.01, 130.11, 129.63, 129.23, 129.16, 128.72, 127.70, 125.82, 125.14, 122.66, 122.59, 118.98, 115.70, 115.48, 44.71; anal. calcd. for $C_{25}H_{17}BrFN_3O_4S$ (554.39): C, 54.16; H, 3.09; N, 7.58. Found: C, 54.35; H, 3.21; N, 7.79%; ESI-MS (m/z): 553.2633 $[M-1]^-$; HPLC purity 97.82%.

2.1.1.4. N-(4-Chlorophenyl)-4-(2-(5-(2-methoxybenzylidene)-2,4-dioxothiazolidin-3-yl) acetamido)benzamide ***15****.*

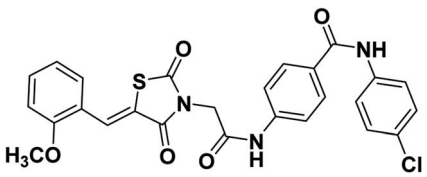

Colorless crystals (yield, 79%); mp = 237–239 °C; IR (KBr) ν cm^{-1}: 3258 (NH), 1745, 1695, 1668 (C=O); ^{1}H NMR (400 MHz, DMSO-d_6) δ ppm: 10.71 (s, 1H, NH), 10.22 (s, 1H, NH), 8.15 (s, 1H, –C=CH), 7.98 (d, J = 8.5 Hz, 2H, Ar–H), 7.81–7.78 (m, 2H, Ar–H), 7.73 (d, J = 8.5 Hz, 2H, Ar–H), 7.55–7.49 (m, 2H, Ar–H), 7.22–7.12 (m, 4H, Ar–H), 4.58 (s, 2H, CH_2), 3.92 (s, 3H, OCH_3); ^{13}C NMR (101 MHz, DMSO-d_6) δ ppm: 169.71, 167.80, 166.80, 166.05, 164.82, 160.42, 143.65, 141.60, 131.08, 129.090, 129.85, 129.82, 128.71, 128.03, 124.44, 123.41, 121.03, 120.78, 117.35, 116.66, 114.36, 58.15, 46.51; anal. calcd. for $C_{26}H_{20}ClN_3O_5S$ (521.97): C, 59.83; H, 3.86; N, 8.05. Found: C, 60.07; H, 4.02; N, 8.23%; ESI-MS (m/z): 520.5674 $[M-1]^+$, 521.5651 $[M]^+$; HPLC purity 100.00%.

2.1.1.5. 4-(2-(5-(2-Methoxybenzylidene)-2,4-dioxothiazolidin-3-yl)acetamido)-N-(4-methoxyphenyl) benzamide ***16****.*

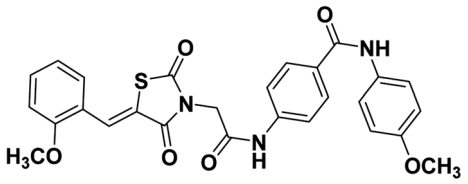

Colorless crystals (yield, 80%); mp = 215–217 °C; IR (KBr) ν cm^{-1}: 3196 (NH), 1700, 1667, 1649 (C=O); ^{1}H NMR (400 MHz, DMSO-d_6) δ 10.69 (s, 1H, NH), 10.0.3 (s, 1H, NH), 8.12 (s, 1H, –C=CH), 7.92 (d, J = 8 Hz, 2H, Ar–H), 7.68 (d, J = 4 Hz, 2H, Ar–H), 7.65 (d, J = 4 Hz, 2H, Ar–H), 7.53–7.48 (m, 2H, Ar–H), 7.19 (d, J = 8 Hz, 1H, Ar–H), 7.12 (t, J = 8, 8 Hz, 2H, Ar–H), 6.91 (d, J = 8 Hz, 2H, Ar–H), 4.54 (s, 2H, CH_2), 3.90 (s. 3H, CH_3), 3.72 (s. 3H, CH_3); ^{13}C NMR (101 MHz, DMSO-d_6) δ ppm: 167.44, 165.44, 164.35, 158.09, 155.45, 141.14, 132.29, 132.29, 129.85, 129.10, 128.66, 121.94, 121.23, 121.12, 121.05, 118.42, 113.71, 112.04, 55.48, 55.17, 44.09; anal. calcd. for $C_{27}H_{23}N_3O_6S$ (517.56): C, 62.66; H, 4.48; N, 8.12. Found: C, 62.53; H, 4.69; N, 8.36%; ESI-MS (m/z): 517.2583 [M]$^+$, 518.2815 [M + 1]$^+$; HPLC purity 100.00%.

*2.1.1.6. 4-(2-(5-(2-Methoxybenzylidene)-2,4-dioxothiazolidin-3-yl)acetamido)-N-(4-nitrophenyl) benzamide **17**.*

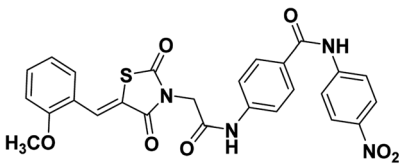

Yellow crystals (yield, 70%); mp = 240–242 °C; IR (KBr) ν cm^{-1}: 3261 (NH), 1745, 1695, 1668 (C=O); ^{1}H NMR (400 MHz, DMSO-d_6) δ 10.77 (s, 1H, NH), 10.72 (s, 1H, NH), 8.27 (d, J = 8.6 Hz, 2H, Ar–H), 8.14 (s, 1H, –C=CH), 8.08 (d, 2H, J = 8 Hz, Ar–H), 8.02 (d, J = 6.8 Hz, 2H, Ar–H), 7.75 (d, J = 6.4 Hz, 2H, Ar–H), 7.50 (dd, J = 8.4, 7.6 Hz, 2H, Ar–H), 7.19 (d, 1H, J = 7.2 Hz, Ar–H), 7.15 (d, 1H, J = 6.4 Hz, Ar–H), 4.58 (s, 2H, CH_2), 3.92 (s, 3H, CH_3). ^{13}C NMR (101 MHz, DMSO-d_6) δ ppm: 167.88, 165.93, 165.88, 164.92, 158.57, 146.10, 142.33, 133.39, 129.62, 129.56, 129.39, 129.21, 125.23, 121.74, 121.55, 121.50, 119.90, 119.00, 112.49, 56.29; anal. calcd. for $C_{26}H_{20}N_4O_7S$ (532.53): C, 58.64; H, 3.79; N, 10.52. Found: C, 58.83; H, 4.01; N, 10.68%; ESI-MS (m/z): 532.5080 [M]$^-$, 533.4765 [M + 1]$^-$; HPLC purity 99.22%.

2.2. Biological examinations

All reagents, solvents, and fine chemicals were obtained from Sigma-Aldrich (Poole, Dorset, UK) and EL NASR Company for intermediate chemicals (Cairo, Egypt). The purity of the purchased materials was more than 98%.

2.2.1. *In vitro* anti-proliferative activity. To assess the inhibitory potential of the synthesized thiazolidine-2,4-dione derivatives **12–17** against the proliferation of MCF-7 and HepG2 cancer cells an *in vitro* MTT assay was applied.[41–43] The cell lines were obtained from VACSERA CO., Dokki, Giza, Egypt. The ESI† file contains further information on this test.

2.2.2. *In vitro* VEGFR-2 inhibition. The synthesized thiazolidine-2,4-dione derivatives **12–17** were subjected to an *in vitro* evaluation against VEGFR-2 *via* the implementation of a VEGFR-2 ELISA kit (VEGFR2(KDR) Kinase Assay Kit Catalog # 40325) (BPS Bioscience, San Diego, USA).[44] The ESI† file contains further information on this test.

2.2.3. Cell cycle analysis. To determine the role of compound **15** in HT-29 cell cycle distribution, cell cycle analysis was performed using propidium iodide (PI) staining and flow cytometry analysis at a concentration of 13.56 μM. The methodologies of this investigation and the used kits were detailed in ESI.†

2.2.4. Apoptosis analysis. The annexin V-FITC and flow cytometry[45–47] technique was utilized to evaluate the ability of compound **15** (at a concentration of 13.56 μM) to induce apoptosis in HT-29 cells. The methodologies of this investigation and the used kits were detailed in ESI.†

2.2.5. BAX, Bcl-2, caspase 8, and caspase 9 and TNF-α and IL-6 determination. The effect of compound **15** (at a concentration of 13.56 μM) on BAX, Bcl-2, caspase 8, caspase 9, TNF-α and IL-6 expression levels in HT-29 cells was evaluated through the use of the RT-qPCR method.[48–52] The procedures and the used kits were illustrated in ESI.†

2.2.6. Statistical analysis. GraphPad Prism version 9 (GraphPad, San Diego, CA, USA) was used to analyze all results. The data were represented as mean ± standard deviation (mean ± SD) from at least three independent experiments (n = 3). One-way analysis of variance (One-way ANOVA) followed by Tukey *post hoc* multiple comparison tests were elected to analyze the significant difference between all groups. $P < 0.05$ was considered statistically significant.

2.3. *In silico* studies

2.3.1. Docking studies. Utilizing docking investigations with MOE2019 software, the potential inhibitory effects of the synthesized thiazolidine-2,4-dione derivatives **12–17** against VEGFR-2 [PDB ID: 2OH4, resolution: 2.05] were assessed. The ESI† file contains further information on this experiment.[15,53]

2.3.2. ADMET studies. ADMET profiles of the synthesized thiazolidine-2,4-dione derivatives **12–17** were evaluated computationally by Discovery Studio 4.0. The ESI† file contains further information on this experiment.[54]

2.3.3. Toxicity studies. The toxicity profiles of the synthesized thiazolidine-2,4-dione derivatives **12–17** were evaluated computationally Discovery Studio 4.0. The ESI† file contains further information on this experiment.[55]

2.3.4. MD simulations. Compound **15**'s capacity to inhibit the VEGFR-2 was examined computationally through MD simulations that were prepared by the CHARMM-GUI web server[56,57] and run using the MD engine GROMACS 2021.[58,59] The ESI† file contains further information on this experiment.

2.3.5. MM-GBSA analysis. MM-GBSA analysis of VEGFR-2-compound **15** complex was evaluated by the Gmx_MMPBSA package.[60,61] The ESI† file contains further information on this experiment.

2.3.6. ProLIF analysis. ProLIF analysis of VEGFR-2-compound **15** complex was evaluated.[62–64] The ESI† file

contains further information on this experiment.

2.3.7. Essential dynamics (ED) analysis. Essential Dynamics (ED) analysis of the VEGFR-2-compound **15** complex was evaluated by GROMACS by utilizing the gmx covar and gmx analog commands.[65] The ESI† file contains further information on this experiment.

2.3.8. Cosine content analysis. Cosine Content analysis of VEGFR-2-compound **15** complex was evaluated by GROMACS.[66] The ESI† file contains further information on this experiment.

2.3.9. Bidimensional projections analysis. Bidimensional Projections analysis of VEGFR-2-compound **15** complex was evaluated by GROMACS.[67,68] The ESI† file contains further information on this experiment.

2.3.10. Density function theory (DFT) calculations. DFT analyses were evaluated for compound **15** by Gaussian software. The ESI† file contains further information on this experiment.[13]

3. Results and discussion

3.1. Chemistry

The synthetic pathways adopted for the synthesis of the target compounds were summarized in Schemes 1–3. Firstly, the starting material thiazolidine-2,4-dione (TZD) **3** was synthesized by a reaction of 2-chloroacetic acid **1** with thiourea **2** under reflux in 4 N HCl.[69] Then, TZD **3** was condensed with various substituted benzaldehydes namely, benzaldehyde **4a**, 2-bromobenzaldehyde **4b**, and 2-methoxybenzaldehyde **4c** in an acidic buffer using sodium acetate along with glacial acetic acid to give the key intermediates **5a–c**, respectively as in adopted procedure.[70] Heating compounds **5a–c** with potassium hydroxide in ethanolic solution yielded the corresponding potassium salts **6a–c**, respectively following the reported procedure[71] (Scheme 1).

On the other hand, 4-aminobenzoic acid **7** was allowed to react with chloroacetyl chloride in DMF to afford the chloroacetamide intermediate **8**. Acylation of compound **8** was performed using thionyl chloride to yield 4-(2-chloroacetamido) benzoyl chloride **9** as described in the reported procedure.[53] Treating of **9** with commercially available amines namely, cyclopentylamine **10a**, 4-chloroaniline **10b**, 4-fluoroaniline **10c**, 4-methoxyaniline **10d**, and 4-nitroaniline **10e** in acetonitrile containing triethylamine (TEA), afforded the target key intermediates **11a–e**, respectively (Scheme 2).

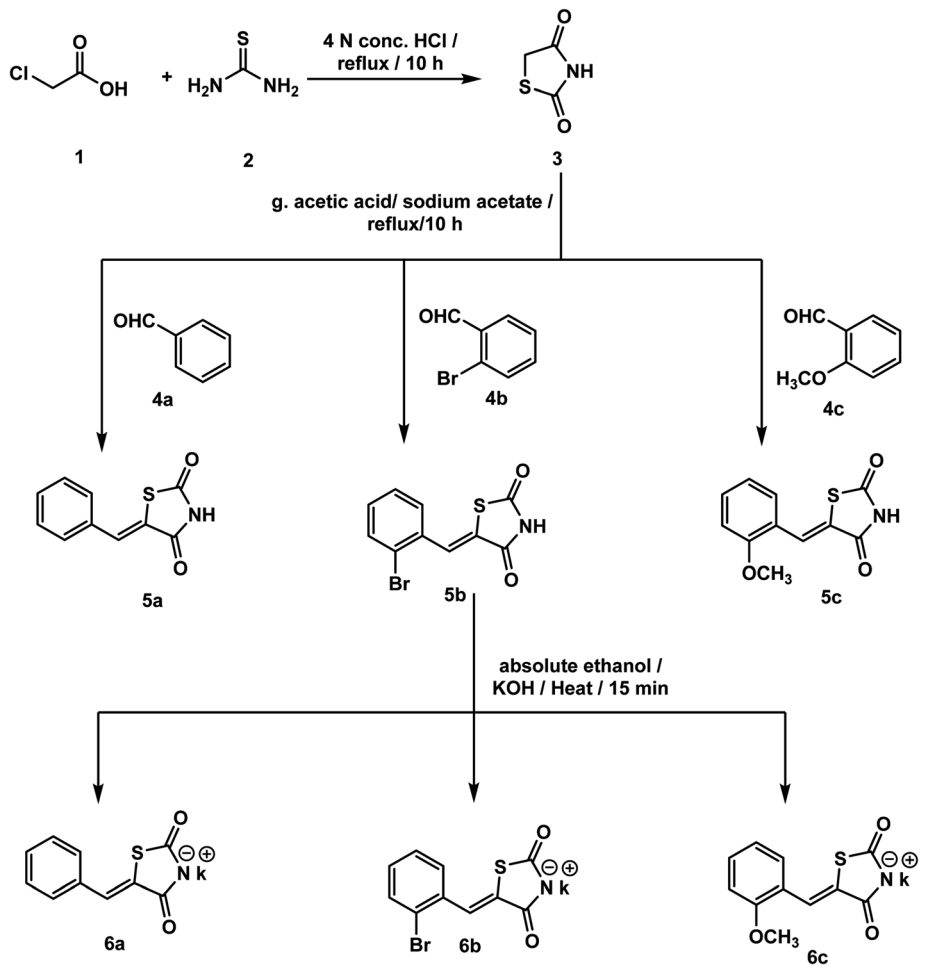

Scheme 1 Synthesis of the key starting materials **6a–c**.

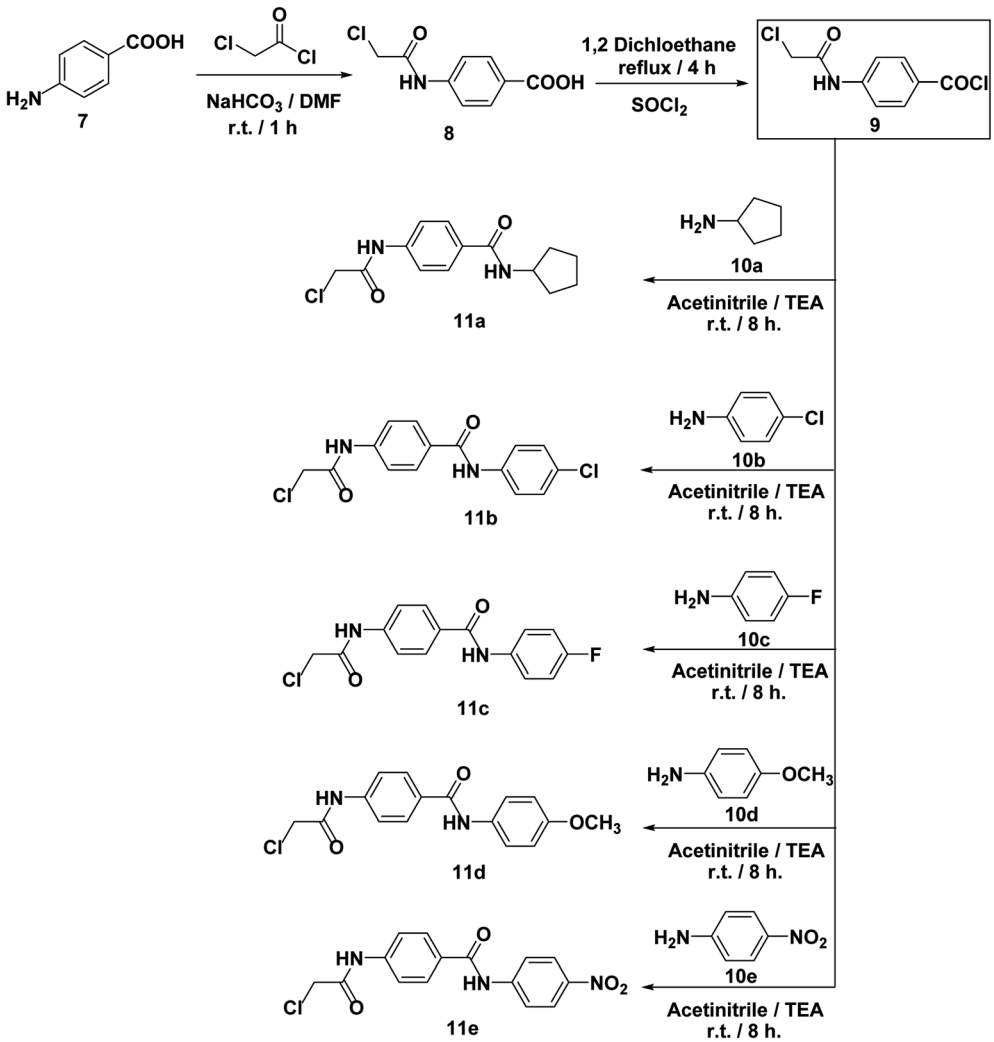

Scheme 2 Synthesis of the key intermediates **11a–e**.

The prepared potassium salts **6a–c** were alkylated with key intermediates **11a–e** *via* heating in dry DMF in the presence of KI to afford the target derivatives **12–17** (Scheme 3).

The IR spectra of the compounds **12–17** presented sharp absorption bands at the ranges of 3258–3196 cm^{-1} and 1745–1649 cm^{-1} confirming the presence of NH and C=O groups, respectively. ^{1}H NMR spectra of compounds **12–17** showed the appearance of shielded singlet signals for the methylene protons as at δ ranges of 4.54–4.61 ppm, and singlet signals around δ ranges of 8.03–8.15 ppm for the benzylidene methine protons. Moreover, their ^{1}H NMR spectra revealed the presence of two NH protons at δ ranges of 8.18–10.72 ppm and 10.63–10.77 ppm. In addition, ^{13}C NMR spectra showed the presence of a methylene carbon in the δ range of 44.64–46.51 ppm. Moreover, the four carbonyl carbons were displayed at the δ range of 164.35–169.71 ppm. This methine was also detected in the ^{13}C NMR spectra at δ of 141.11–142.33 ppm.

The purity of the synthesized compounds was detected using HPLC to be more than 95% for all compounds. Additionally, elemental analysis indicated that the calculated % of CHN for all compounds were in the range of ±0.4%. Such findings reflect the high purity index of the synthesized members.

3.2. Biological evaluation

3.2.1. *In vitro* anticancer effects and VEGFR-2 enzyme assay. Compounds **12–17** were tested for antiproliferative activity against three human cancer cell lines: HT-29 (colon cancer cell line), A-549 (epithelial cancer cell line), and HCT-116 (colon cancer cell line) using the MTT assay. Sorafenib was fixed as a positive control. The dose–response curves for the obtained IC_{50} values against all cell lines were calculated using GraphPad Prism version 9 as presented in ESI.†

In general, compound **15** was the most potent derivative against HT-29, A-549, and HCT-116 cell lines, with IC_{50} values of 13.56,17.80, 13.84 μM, respectively, compared to sorafenib which showed IC_{50} values of 8.826 ± 0.33, 6.900 ± 0.29, and 5.813 ± 0.21 μM against HT-29, A-549, and HCT-116, respectively.

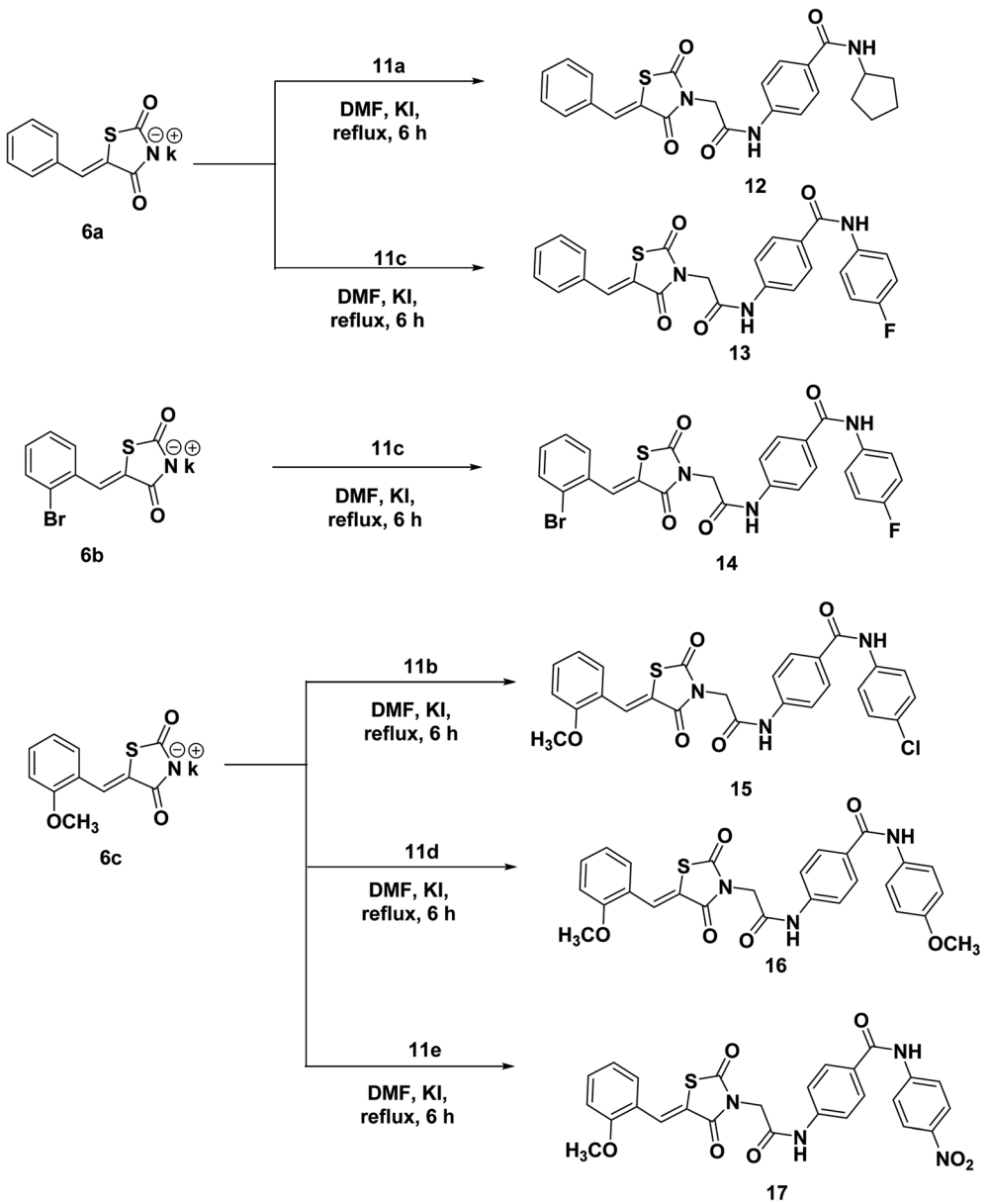

Scheme 3 Synthesis of the target compounds **12–17**.

Table 1 IC_{50} values of the new compounds **12–17** against HT-29, A-549, HCT-116, and VEGFR-2

	IC_{50}[a] (μM)			
Comp.	HT-29	A549	HCT-116	VEGFR-2 IC_{50}[a] (μM)
12	17.26 ± 1.02	18.77 ± 1.30	N/A	0.477 ± 0.02
13	27.94 ± 1.75	19.39 ± 1.22	18.76 ± 1.07	0.157 ± 0.007
14	22.27 ± 1.60	19.81 ± 1.28	28.98 ± 2.11	1.586 ± 0.067
15	13.56 ± 1.09	17.80 ± 0.93	13.84 ± 1.05	0.081 ± 0.003
16	18.55 ± 1.11	24.81 ± 1.55	28.91 ± 1.83	1.152 ± 0.048
17	47.21 ± 2.55	10.89 ± 0.69	9.17 ± 0.55	0.976 ± 0.041
Sorafenib	8.826 ± 0.33	6.900 ± 0.29	5.813 ± 0.21	0.061 ± 0.002

[a] The results are the mean of three experiments.

Respecting HT-29, compound **15** demonstrated the superior anticancer result, with an IC_{50} value of 13.56 μM. Derivatives **12** and **16** showed strong IC_{50} values of 17.26 and 18.55 μM, respectively. Derivatives **13**, **14**, and **17** presented mild cytotoxicity with IC_{50} values ranging from 22.27 to 47.21 μM.

Additionally, derivatives **15** and **17** demonstrated very good activities towards the A549 cell lines with IC_{50} values of 17.8 and 10.89 μM, respectively. Furthermore, the remained derivatives showed good cytotoxicity with IC_{50} values ranging from 18.77 to 24.81 μM.

Relating to HCT-116, compounds **15** and **17** have proven the highest anticancer activities, with IC_{50} values of 13.84 and 9.17 μM, respectively. Derivatives **13**, **14** and **16** showed good cytotoxicity with IC_{50} values of 18.76, 28.98, and 28.91 μM, respectively. On the other hand, compound **12** was inactive against the HCT-116.

Furthermore, all compounds were *in vitro* evaluated for enzymatic inhibitory activity against VEGFR-2. The inhibitory activity was measured using sorafenib as a reference inhibitor and expressed as IC_{50} in μM. The data shown in Table 1 demonstrated that the thiazolidine-2,4-dione derivative **15** revealed very potent VEGFR-2 inhibitory action with IC_{50} value of 0.081 μM, compared to sorafenib (IC_{50} = 0.061 μM). The other compounds showed moderate activities against VEGFR-2 with IC50 values ranging from 0.157 to 1.586 μM.

Table 2 IC_{50} values of the new compounds **12–17** against Vero normal cells and selectivity indices against the tumor cells

		Selectivity index		
Comp.	Vero cells IC_{50} (μM)	HT-29	A549	HCT-116
12	422.29 ± 6.17	24.47	22.50	
13	425.65 ± 2.42	15.23	21.95	22.69
14	491.03 ± 4.97	22.05	24.79	16.94
15	389.62 ± 2.95	28.73	21.89	28.15
16	123.28 ± 1.44	6.65	4.97	4.26
17	178.8 ± 1.67	3.79	16.42	19.50

3.2.2. Structure–activity relationship (SAR). The results of VEGFR-2 inhibitory activities gave important notes about the

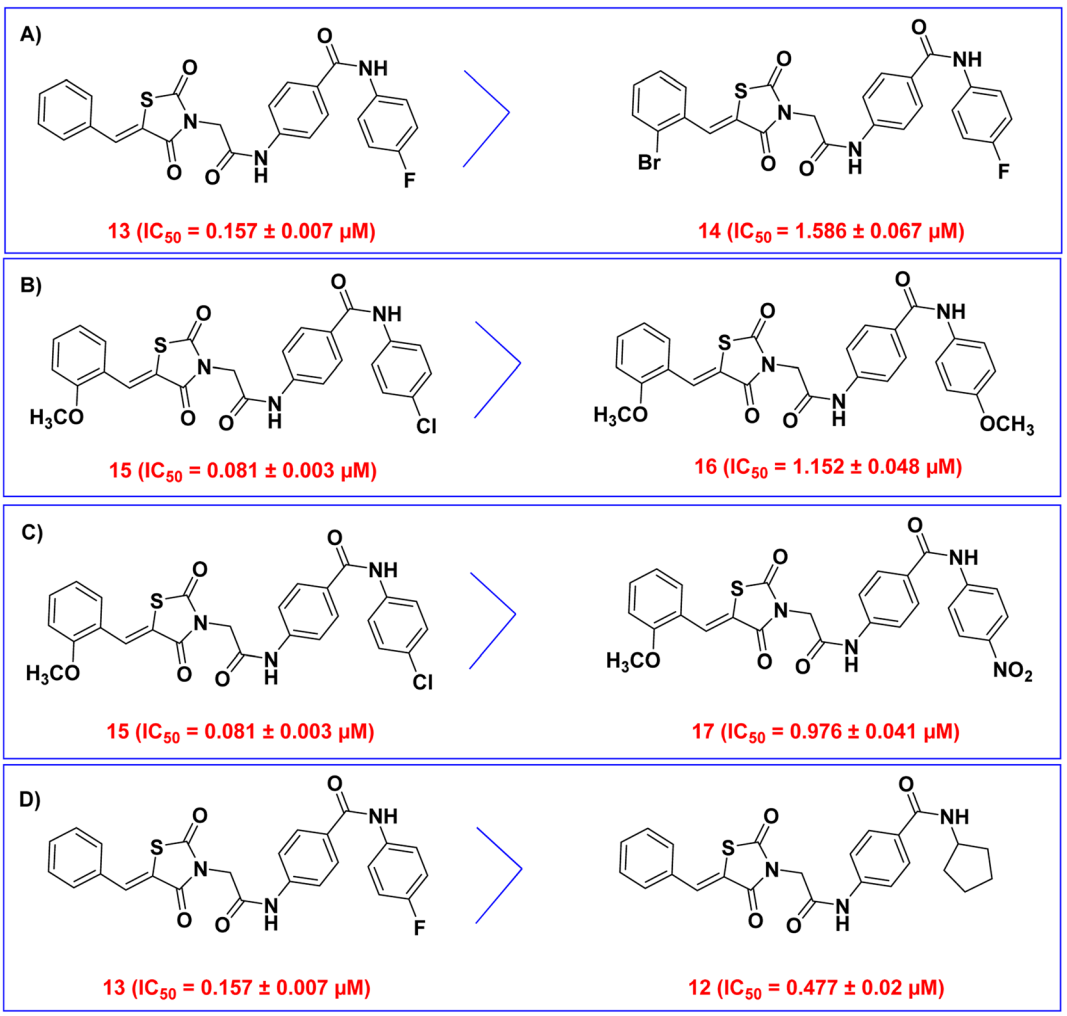

Fig. 3 SAR of the synthesized thiazolidine-2,4-diones as VEGFR-2 inhibitors. (A) Comparison between compounds **13** and **14**. (B) Comparison between compounds **15** and **16**. (C) Comparison between compounds **15** and **17**. (D) Comparison between compounds **13** and **12**.

SAR as follows. First, we investigated the impact of substitution on the (*Z*)-5-benzylidenethiazolidine-2,4-dione moiety. Accordingly, the activity of compound **13** ($IC_{50} = 0.157 \pm 0.007$ μM) was compared with the activity of the corresponding compound **14** ($IC_{50} = 1.586 \pm 0.067$ μM). As observed, compound **13** is more active than compound **14** as a VEGFR-2 inhibitor. This revealed that unsubstituted (*Z*)-5-benzylidenethiazolidine-2,4-dione moiety is more beneficial than the bromo derivative (Fig. 3A).

Then, we examined the electronic and hydrophobic effect of the hydrophobic tail on VEGFR-2 inhibitory activity. To examine the electronic effect, we compared the activities of compounds **15** (incorporating 4-chlorophenyl), **16** (incorporating 4-methoxy phenyl), and **17** (incorporating 4-nitrophenyl). It was found that compounds **15** and **17** are more active than compound **16.** This indicated that the substitution of the terminal phenyl ring with an electron-withdrawing group (Cl and NO_2) is more advantageous than the substitution with an electron-donating group (OCH_3) (Fig. 3B).

For the hydrophobic effect, it was found that compound **15** (4-Cl) is more active than compound **17** (4-NO_2). This revealed that the substitution of the terminal phenyl ring with a hydrophobic group (Cl) is more helpful than the substitution with a hydrophilic group (NO_2) (Fig. 3C).

Next, the planarity effect of the hydrophobic tail on VEGFR-2 inhibitory activity was investigated. By comparing the activity of compound **13** (incorporating 4-fluorophenyl as sp^2 hybridized moiety) and compound **12** (incorporating cyclopentyl as sp^3 hybridized moiety), it was found that compound **13** is more active than compound **12**. This indicated that the planarity of the hydrophobic tail (sp^2 hybridization) is more valuable than the non-planarity (sp^3 hybridization) (Fig. 3D).

3.2.3. *In vitro* cytotoxicity against Vero normal cell line. One of the biggest issues with cancer treatment is the

Table 3 Effect of compound **15** and sorafenib on HT-29.cell cycle progression

	Cell cycle distribution (%)		
Sample	% G0-G1	% S	% G2/M
Compound 15/HT-29	58.26 ± 1.74	33.04 ± 2.22[a]	8.70 ± 0.6[a]
Sorafenib/HT-29	51.95 ± 1.05[a,b]	41.06 ± 1.49[a,b]	6.99 ± 1.01[a,b]
Control HT-29	61.44 ± 1.56	25.82 ± 0.62	12.74 ± 1.7

[a] Significant *P* value from control HT-29. [b] Significant *P* value from compound **15**/HT-29, significant *P* value <0.05 & by using One-way ANOVA followed by Tukey's *post hoc* multiple comparison tests.

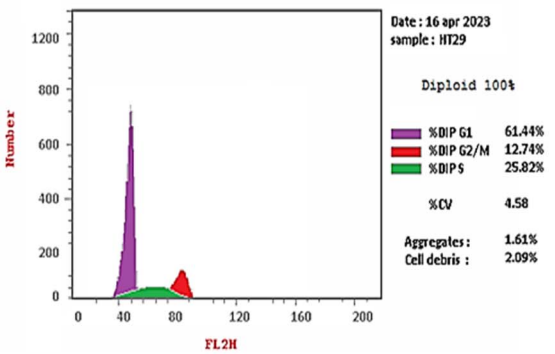

(**A**) Control (HT-29) cells

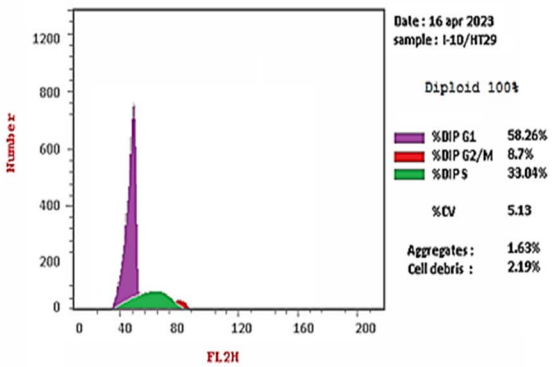

(**B**) Compound **15**/ HT-29

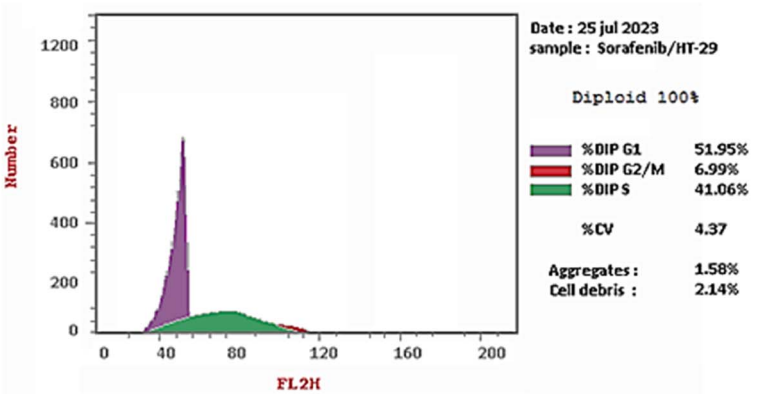

(**C**) Sorafenib/ HT-29

Fig. 4 Cell cycle distribution of HT-29 cells as determined by flow cytometry. (A) Control cells, (B) compound **15**, (C) sorafenib.

Table 4 The impact of compound **15** and sorafenib on the various stages of cell death in HT-29 cells

Sample	Total apoptosis	Early apoptosis	Late apoptosis	Necrosis
Compound 15/HT-29	31.44 ± 1.56^{a}	9.11 ± 0.36^{a}	16.52 ± 0.89^{a}	5.81 ± 0.31^{a}
Sorafenib/HT-29	$46.28 \pm 2.22^{a,b}$	$14.61 \pm 0.89^{a,b}$	$26.82 \pm 1.02^{a,b}$	$4.85 \pm 0.31^{a,b}$
Control HT-29	3.06 ± 0.24	0.69 ± 0.06	0.21 ± 0.08	2.16 ± 0.1

[a] Significant *P* value from control HT-29. [b] Significant *P* value from compound **15**/HT-29, significant *P* value < 0.05 & by using one-way ANOVA followed by Tukey's *post hoc* multiple comparison tests.

unintended harm to healthy cells brought on by the high toxicity of anticancer agents. Therefore, the cytotoxicity of the synthesized derivatives was examined *in vitro* using normal cell lines to explore whether they were more hazardous to cancer cells than normal cells. The results revealed that the synthesized compounds showed noticeable safety profiles on normal non-cancer (Vero) cells where these derivatives displayed cytotoxic IC_{50} values ranging from 123.28 to 491.03 μM (Table 2). Such values were very high when compared to the values against the three cancer cell lines that were ranging from 9.17 to 47.21 μM. This indicated the safety profile and selectivity of compounds **12–17** towards cancer cell lines.

For selectivity indices against tumor cell lines, the synthesized derivatives showed selectivity indices ranging from 3.79 to 28.73. The most active compound **15** showed the highest selectivity indices of 28.73, 21.89, and 28.15 against HT-29, A549, and HCT-116, respectively. This indicated the high safety margin of compound **15**. So, this compound was selected for further mechanistic studies.

3.2.4. Cellular mechanistic studies

3.2.4.1. Cell cycle analysis. The most promising compound in this investigation, compound **15**, was incubated with HT-29 cells (chosen as the most sensitive cancer cell line) for 72 h at a concentration of 13.56 μM (IC_{50} against HT-29 cells). Sorafenib was fixed as a positive control. The different stages of the cell cycle in the HT-29 cells were then examined using flow cytometry analysis before and after treatment. Compound **15** and sorafenib were shown to raise the proportion of cells in the S phase from 25.82% in control cells to 33.04 and 41.06%, respectively. Moreover, compound **15** and sorafenib decrease

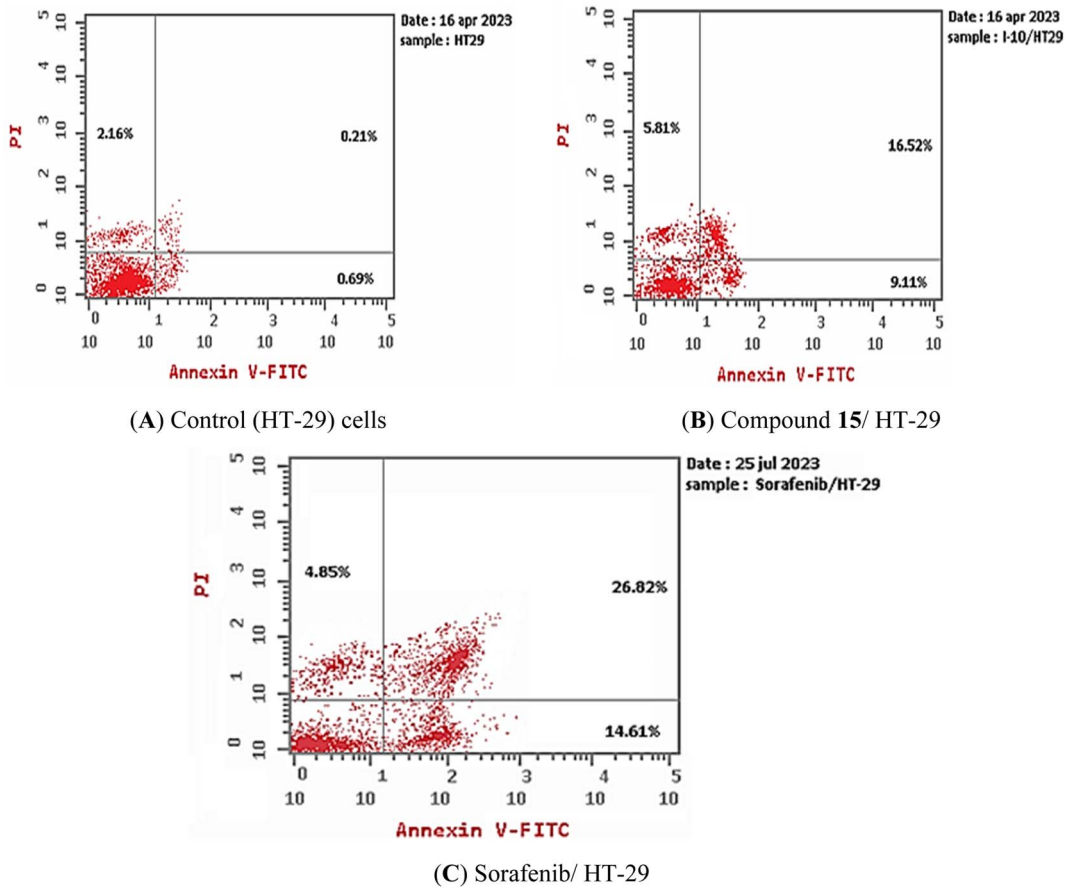

Fig. 5 Compound **15** induced apoptosis in HT-29 cells. (A) Control and (B) compound **15**, (C) sorafenib.

Table 5 Effects of compound **15** and sorafenib on the expression levels of BAX, Bcl-2, caspases-8, and caspases-9 in HT-29 cells

	Gene expression (Fold Change)			
Sample	BAX	Bcl-2	Caspase-8	Caspase-9
Compound 15/HT-29	4.858 ± 0.132^{a}	0.347 ± 0.033^{a}	1.701 ± 0.029^{a}	3.247 ± 0.085^{a}
Sorafenib/HT-29	4.900 ± 0.20^{a}	0.316 ± 0.016^{a}	$3.682 \pm 0.35^{a,b}$	$4.972 \pm 0.13^{a,b}$
Control HT-29	1	1	1	1

[a] Significant *P* value from control HT-29. [b] Significant *P* value from compound **15**/HT-29, significant *P* value < 0.05 & by using one-way ANOVA followed by Tukey's *post hoc* multiple comparison tests.

the percentage of cells in the G0-G1 phase from 61.44% in control cells to 58.26 and 51.95%, respectively. As well, in the G2/M phase the percentage of cells was dropped from 12.74% in control cells to 8.70 and 6.99% for cells that had been treated with compound **15** and sorfenib, respectively (Table 3 and Fig. 4). These findings revealed that compound **15** may arrest the HT-29 cells at S phase.

Table 6 Effects of compound **15** and sorafenib on the expression levels of TNF-α and IL6 in HT-29 cells

	(Fold Change)	
Sample	TNF-α	IL6
Compound 15/HT-29	$0.570 \pm 0.02^{a\#}$	0.202 ± 0.021^{a}
Sorafenib/HT-29	$0.2461 \pm 0.016^{a,b}$	$0.2836 \pm 0.022^{a,b}$
Cont. HT-29	1	1

[a] Significant *P* value from control HT-29. [b] Significant *P* value from compound **15**/HT-29, significant *P* value < 0.05 & by using one-way ANOVA followed by Tukey's *post hoc* multiple comparison tests.

3.2.4.2. Apoptosis assay. Using flow cytometry and Annexin V (FITC-conjugated) apoptosis detection kits, compound **15**'s capacity to induce apoptosis in HT-29 cell lines was evaluated. HT-29 cells were exposed to compound **15** at a concentration of 13.56 μM (IC_{50} against HT-29 cells) for 72 h. Sorafenib was fixed as a positive control. Compound **15** and sorafenib caused overall apoptosis of 31.44% and 46.28, respectively, compared to 3.06% for control HT-29 cells, as seen in Table 4 and Fig. 5. Comparing to the control, which had early and late apoptosis percentages of 0.69% and 0.21%, compound **15** and sorafenib unambiguously increased the early apoptosis by 9.11% and 14.61% while augmented the late apoptosis by 16.52 and 26.82%, respectively. This demonstrates that the anticancer properties of the most promising candidate (compound **15**) may be attributed to its ability to induce programmed apoptosis.

3.2.4.3. Effects on Bcl-2 family proteins and caspases. The effects of compound **15** at a concentration of 13.56 μM (IC_{50} against HT-29 cells). On the levels of BAX, Bcl-2, caspase-8, and caspase-9 expression in MCF-7 cells were investigated using RT-qPCR. Sorafenib was fixed as a positive control. The findings

Table 7 The binding energies (Δ*G*) of the synthesized thiazolidine-2,4-dione derivatives and sorafenib against VEGFR-2

Comp.	Δ*G* [kcal mol^{-1}]	(Number of H-bonds)/amino acids	Number of hydrophobic bonds/ amino acids
Sorafenib	−21.33	(5)/Cys917, Glu88, and Asp1044	(8)/Leu838, Ala864, Leu1033 Val914, Val846, Cys1043, Phe1045. Leu887, His1024, and Leu1017
12	−21.95	(3)/Cys917, Glu88, and Asp1044	(8)/Leu838, Phe916, Ala864, Leu1033, Val914, Val897, Phe1045, and Ile886
13	−21.84	(3)/Cys917, Glu88, and Asp1044	(9)/Leu838, Phe916, Ala864, Leu1033, Val914, Val897, Cys1043, Leu887, and Ile886
14	−24.15	(3)/Cys917, Glu88, and Asp1044	(9)/Leu838, Phe916, Ala864, Leu1033, Val914, Val897, Cys1043, and Ile886
15	−24.62	(3)/Cys917, Glu88, and Asp1044	(8)/Leu838, Phe1045, Ala864, Leu1033, Val914, Val897, Cys1043, Leu887, and Ile886
16	−24.05	(3)/Cys917, Glu88, and Asp1044	(8)/Leu838, Phe916, Ala864, Leu1033, Val914, Val897, Phe1045, Cys1043, and Leu887
17	−23.16	(3)/Cys917, Glu88, and Asp1044	(8)/Leu838, Phe1045, Ala864, Leu1033, Val914, Val897, Phe1045, Cys1043, Ile886, and Ile886

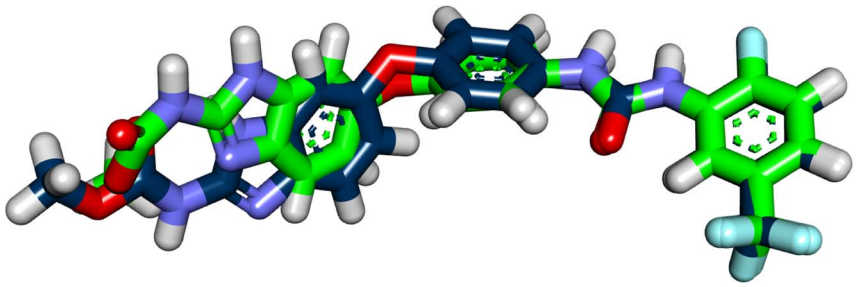

Fig. 6 RMSD value of 1.17 Å between the original ligand (dark blue) and the docked one (green) during the validation process of the docking studies.

demonstrated that compound **15** and sorafenib enhanced the pro-apoptotic protein BAX level by 4.8 and 4.9-folds, respectively when compared to the control. Furthermore, compound **15** and sorafenib markedly decreased Bcl-2 levels, an anti-apoptotic protein, by 2.8 and 3.1-folds when compared to the control. Additionally, the data showed a 1.7 and 3.6-folds rise in caspase-8 levels in compound **15** and sorafenib, respectively, compared to the control. In addition, compound **15** and sorafenib significantly increased caspase-9 levels by 3.24 and 4.97-folds in comparison to the control (Table 5).

3.2.4.4. TNF-α and IL-6 inhibition. Chronic inflammation has been identified as a vital contributing factor to the progression and development of several types of cancer.[72] Inflammatory mediators such as chemokines and cytokines played a crucial role in the promotion of cancer cell growth, survival, and metastasis by suppressing immune surveillance, inducing angiogenesis, and causing DNA damage. Additionally, inflammatory mediators have been reported to induce the upregulation of VEGF expression through several intracellular signaling pathways showing synergistic effects to potentiate VEGF expression and enhance its pro-angiogenic effect.[73] Furthermore, several studies have confirmed that VEGFR-2 inhibitors can decrease the production of pro-inflammatory cytokines in several cell types such as tumor necrosis factor-α (TNF-α)[74] and interleukins (ILs).[75,76]

The inhibitory effects of compound **15** at a concentration of 13.56 μM (IC_{50} against HT-29 cells) against TNF-α and IL6 in HT-29 cells were observed using the RT-qPCR technique. Sorafenib was fixed as a positive control. According to Table 6, compound **15** and sorafenib considerably lowered the levels of TNF-α by 1.7 and 4-folds, respectively. Moreover, the IL-6 levels were markedly reduced by compound **15** and sorafenib by 4.9 and 3.5-folds, respectively in comparison to control HT-29 cells.

3.3. Computational studies

3.3.1. Molecular docking. Docking studies were carried out for the synthesized compounds against the crystal structure of VEGFR-2 (PDB ID: 2OH4). MOE2019 software was utilized in these experiments. To standardize the binding pattern, sorafenib was utilized as a reference VEGFR-2 inhibitor. The binding modes as well as the binding energies (Δ*G*) of the synthesized compounds and sorafenib were deeply discussed.

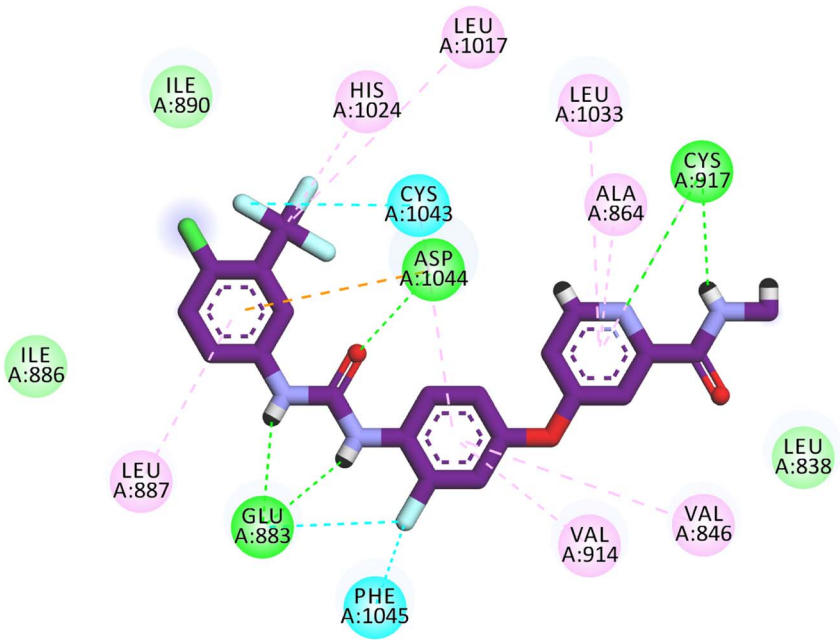

Fig. 7 Binding mode of sorafenib against VEGFR-2.

Table 7 summarizes the binding energies (ΔG) of the synthesized compounds and sorafenib.

As validation of the docking procedure is essential, the co-crystallized ligand was docked against the active site. Then the RMSD value between the docked and original ligand was calculated. From Fig. 6, it was clear that the RMSD value is very low (1.17 Å) due to the complete superimposition of the two ligands. The low RMSD value and complete superimposition of the original and docked ligands indicated the validity of the docking process.

Sorafenib occupied the different pockets of the active site forming five hydrogen bonds with the crucial amino acids

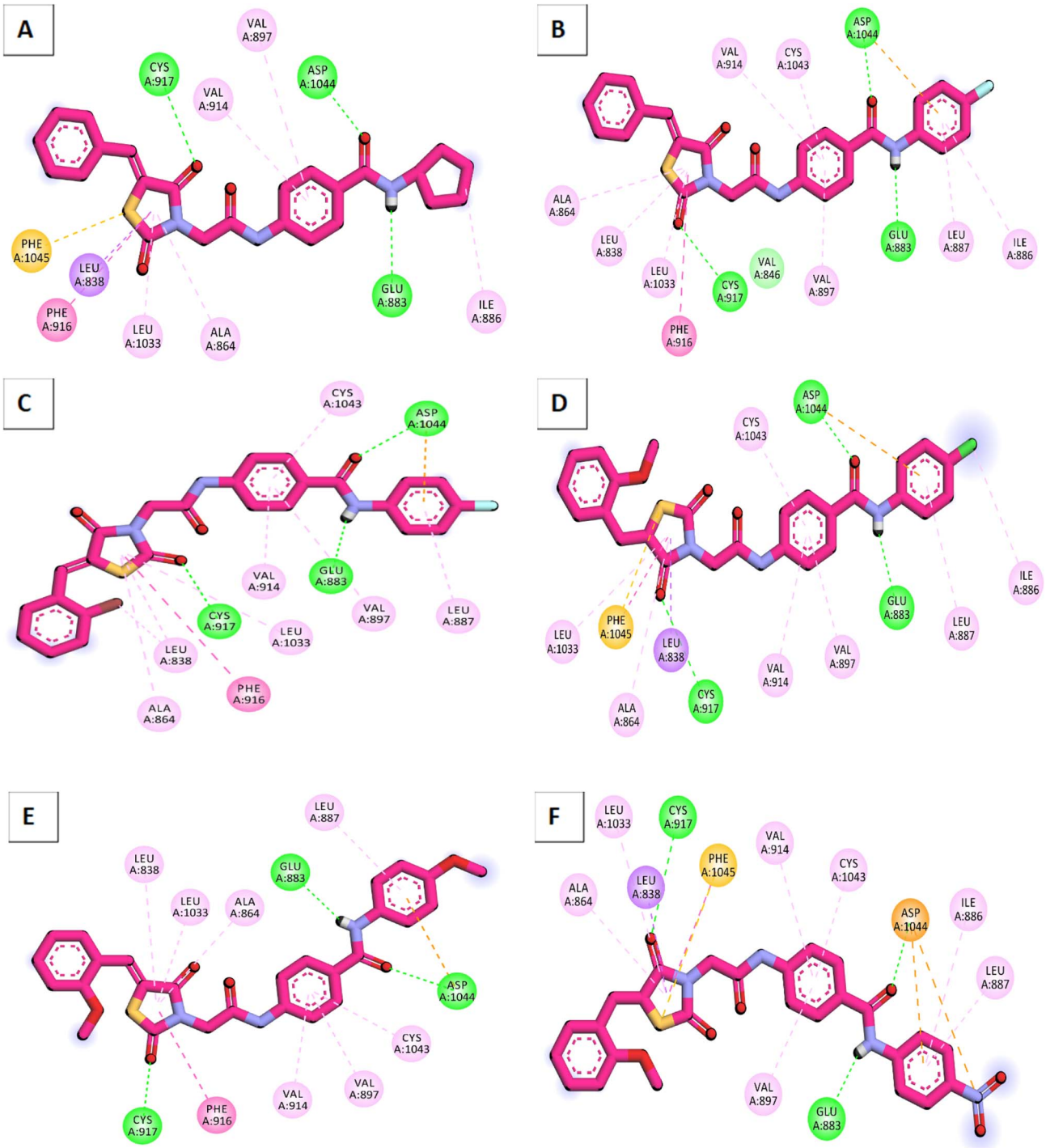

Fig. 8 Binding modes of the synthesized compounds against VEGFR-2. (A) Compound **12**, (B) compound **13**, (C) compound **14**, (D) compound **15**, (E) compound **16**, (F) compound **17**.

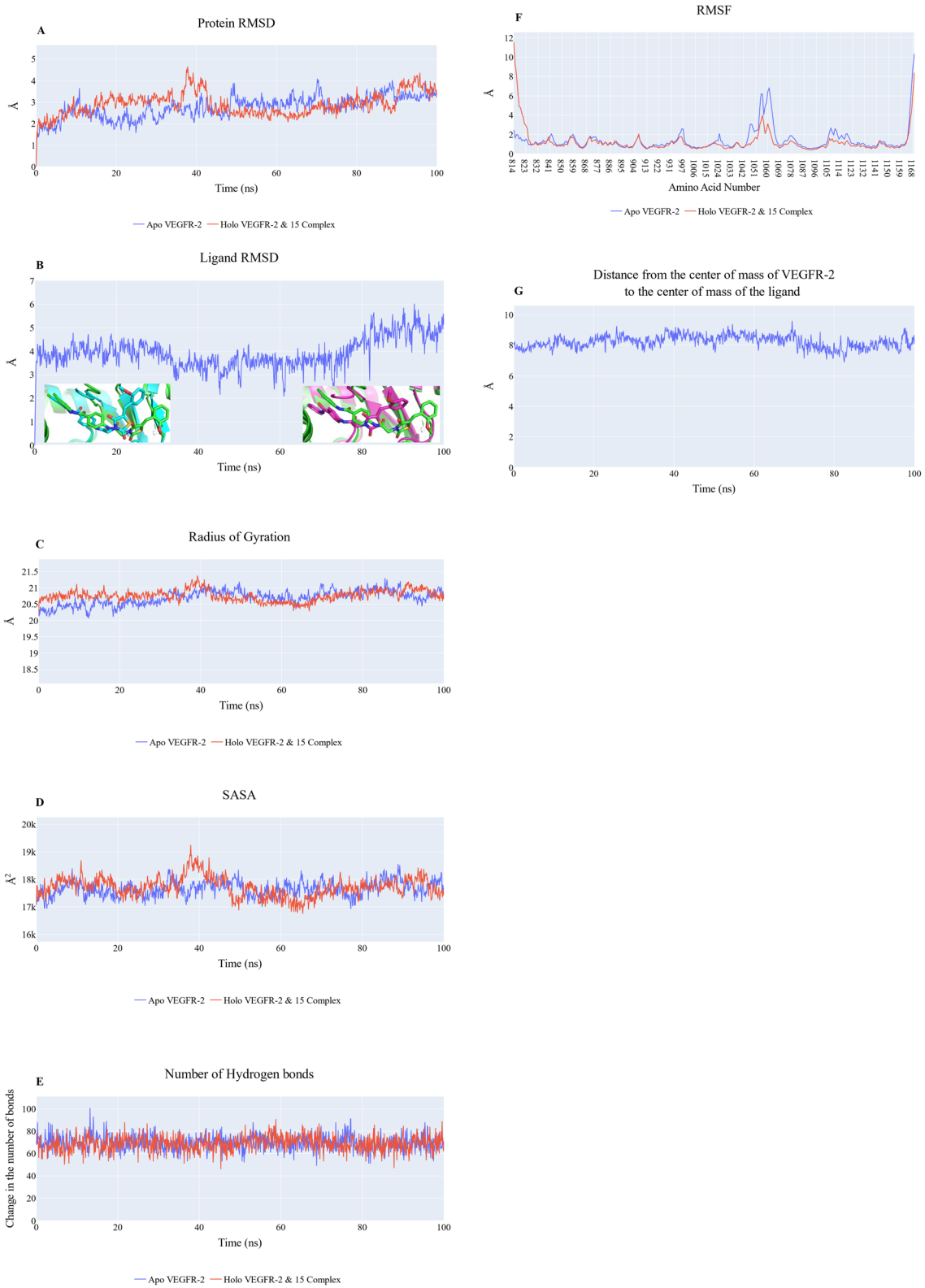

Fig. 9 MD simulation of compound 15_VEGFR-2 complex. (A) RMSD values from the trajectory for the VEGFR-2 protein in apo (blue line) and holo forms (red line), (B) compound **15** RMSD values. The insets show a comparison between the initial ligand structure (0 ns; green sticks) with) compound **15** at 18.2 ns (cyan sticks) and 85 ns (magenta sticks), (C) radius of gyration for the VEGFR-2 protein in apo (blue line) and holo forms (red line), (D) SASA for the VEGFR-2 protein in apo (blue line) and holo forms (red line), (E) change in the number of H-bonds for the VEGFR-2 protein in apo (blue line) and holo forms (red line), (F) RMSF for the VEGFR-2 protein in apo (blue line) and holo forms (red line), (G) distance from the center of mass of compound **15** and VEGFR-2 protein.

Cys917, Glu88, and Asp1044 at the hinge region and the DFG motif region. In addition, sorafenib showed many hydrophobic interactions at the different pockets. It exhibited an energy binding of -21.33 kcal mol^{-1} (Fig. 7).

According to an analysis of the docking results, the synthesized compounds were able to pinpoint the VEGFR-2 kinase ATP binding site and interact with its critical amino acids similarly to sorafenib. In addition, these compounds showed the same orientation of sorafenib inside the active pocket. Their binding energies were illustrated in Table 7. In detail, the 5-benzylidenethiazolidine-2,4-dione moiety of the synthesized compounds occupied the hinge regions of the active site forming essential interactions with the crucial amino acid Cys917. In addition, the phenylacetamide (linker) moiety was oriented into the gatekeeper region of the active site forming many hydrophobic interactions. These interactions have a great role in the stabilization of the tested compounds in the active site. Furthermore, through their amide group, all the tested molecules formed two hydrogen bonds with Glu883 and Asp1044 in the DFG motif region. These interactions are essential for maximal fitting in the active site. Finally, the terminal hydrophobic tails (cyclopentyl, 4-flurophenyl, 4-chlorophenyl, 4-methoxyphenyl, and 4-nitrophenyl) of the synthesized compound occupied the allosteric pocket of the active site forming many hydrophobic bonds. Some of them formed some electrostatic attractions with Asp1044 as shown in Fig. 8.

3.3.2. Molecular dynamic (MD) simulation. MD simulations studies were performed to examine the dynamic and energetic changes that were happened after the binding of compound **15** with VEGFR-2. It was determined through analyses of a 100 ns production run that compound **15** maintained a nearly constant conformation and distance from the protein's center of mass throughout the simulation. After 10 ns, the RMSD values for apo (blue line) and holo protein (red line) are shown to have equilibrated at about 2.7 Å and 2.9 Å, respectively (Fig. 9A). Fig. 9B demonstrates a relatively moderate RMSD (3.9 Å on average) for the compound **15**. The moderately large value and the rise in the last 20 ns are due to the ligand's conformational change inside the binding pocket, as seen in the two insets of Fig. 9B. Compound **15** at 18.2 ns (cyan) and 85 ns (magenta) was compared to the starting frame (green sticks). The average radius of gyration of the apo and holo systems is around 20.7 Å, as seen in Fig. 9C. As can be observed in Fig. 9D,

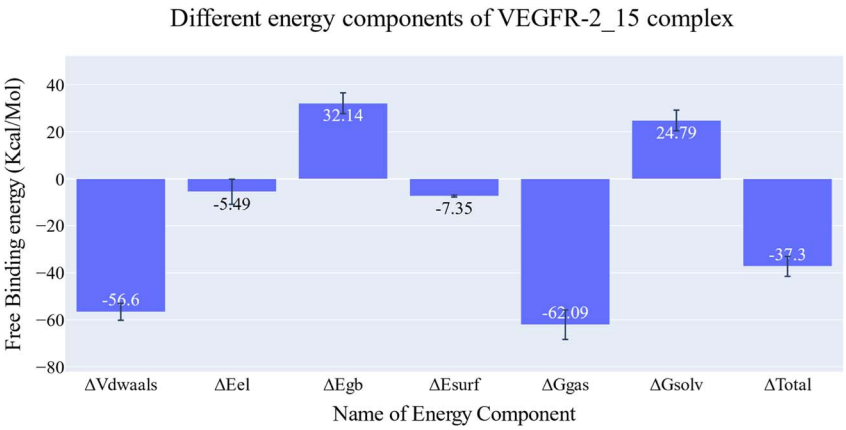

Fig. 10 MM-GBSA energetic components and their values. Bars represent the standard deviations.

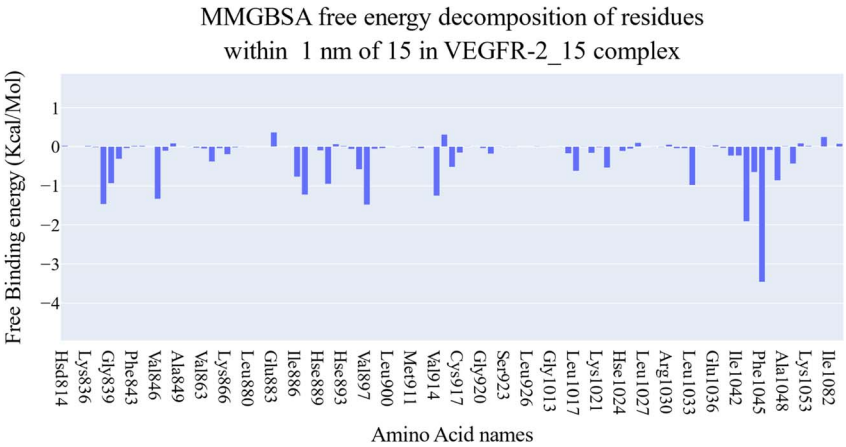

Fig. 11 The binding free energy decomposition of the VEGFR-2_**15** complex.

the average SASA values for the apo and holo proteins are 17656 Å^2 and 17716 Å^2, respectively. Fig. 9E shows that the overall number of H-bonds changes with an average of around 70 bonds in each system. Overall, this would suggest that the structure of the protein is stable. The RMSF plot (Fig. 9F) reveals that amino acids are highly stable (have fluctuation values of less than 2 Å), except for the N-terminus for the holo protein (11.5 Å), the Tyr994:Asp996 loop of the apo system (2.5 Å), the Gly1046:Leu1065 loop of the apo system (6.6 Å), Lys1053:Asp1062 for the holo protein (4.0 Å), the Pro1106:Ile1112 loop of the apo protein (2.6 Å), and the C-terminus (10.3 Å for the apo protein and 8.3 Å for the holo protein). Strong binding stability is indicated by the stable separation between the center of mass of the ligand and the protein with an average distance of 8.2 Å (Fig. 9G).

3.3.3. MM-GBSA studies. Fig. 10 shows the MM-GBSA-calculated components of the binding free energy. The binding energy of compound **15** is −37.3 kcal mol^{-1} on average, indicating an extremely strong interaction. Electrostatic interactions (−5.49 kcal mol^{-1}) contribute to binding stability, although considerably less than van der Waals interactions (−56.6 kcal mol^{-1}). Using a decomposition analysis of the free energy, the contribution of amino acids within 1 nm of compound **15** molecule was calculated (Fig. 11). Leu838 (−1.46 kcal mol^{-1}), Val846 (−1.33 kcal mol^{-1}), Leu887 (−1.22 kcal mol^{-1}), Val897 (−1.48 kcal mol^{-1}), Val914 (−1.25 kcal mol^{-1}), Cys1043 (−1.91 kcal mol^{-1}), and Phe1045 (−3.45 kcal mol^{-1}) are the amino acids that have a contribution less than −1 kcal mol^{-1}.

3.3.4. ProLIF python & PLIP studies. Very long-lasting hydrophobic interactions (91.1% incidence or greater) are detected between Leu838, Val846, Leu887, Ile890, Val897, Val914, Cys1022, Cys1043, Asp1044, and Phe1045 and compound **15** using the ProLIF library (Fig. 12A–C). In addition, Asp1044 creates H-bonds with compound **15** for roughly half of the simulation duration (53.2%). The representative frames

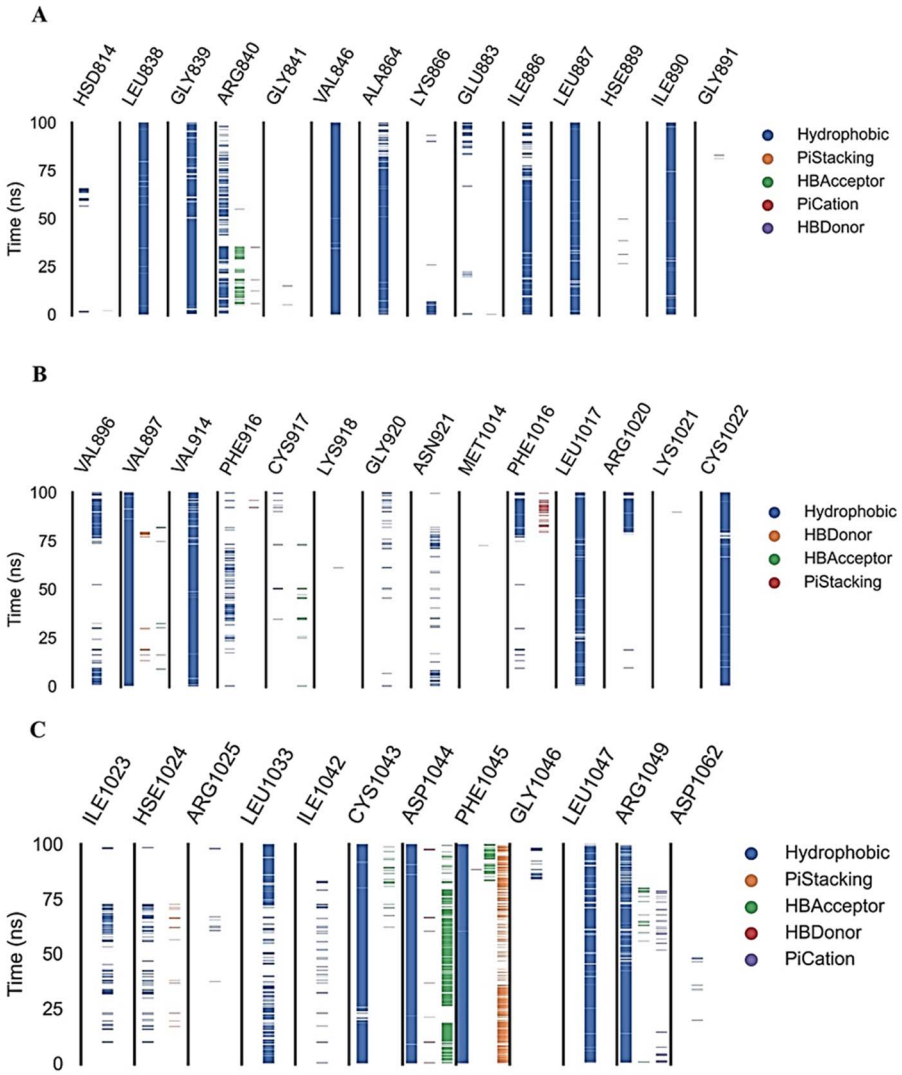

Fig. 12 Amino acids, types of interactions with compound **15**, and their occurrence during the whole simulation time using the ProLIF python library.

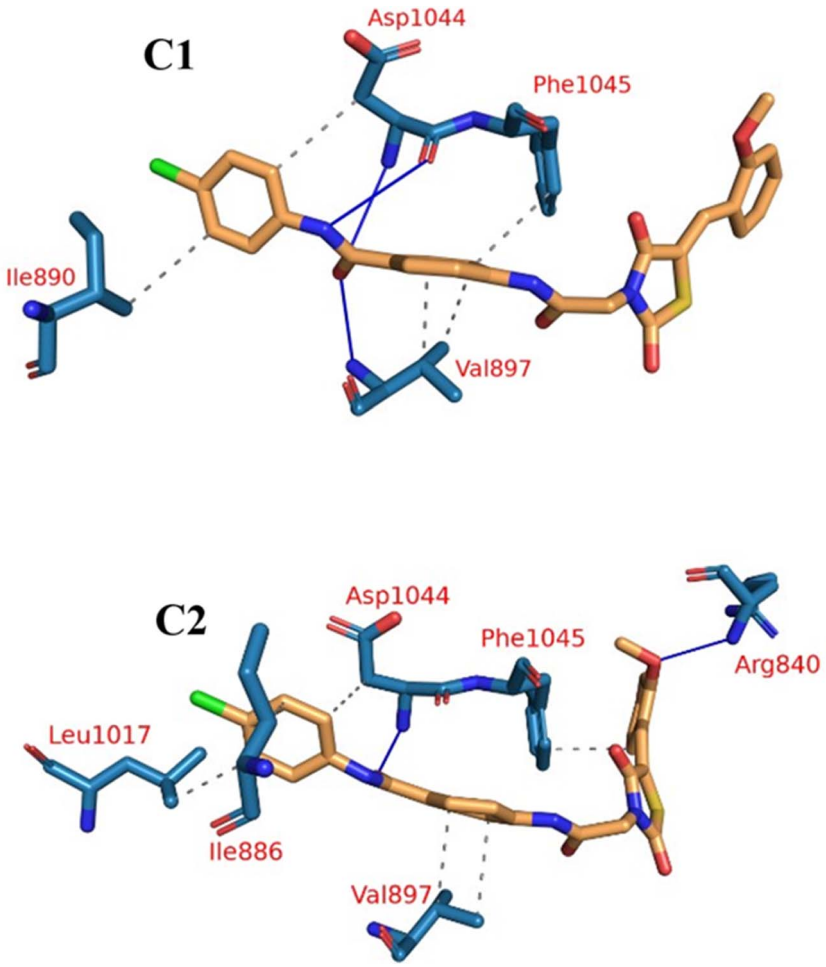

Fig. 13 The two clusters representative obtained from TTClust and their 3D interactions with compound **15**. Grey dashed lines: hydrophobic interactions, blue solid lines: H-bonds, orange sticks: compound **15**, blue sticks: amino acids of VEGFR-2 protein.

obtained from clustering were then run *via* PLIP to calculate interactions and extract 3D binding conformations as .pse files (Fig. 13).

3.3.5. PCA analysis. The principal component analysis helped us study the trajectory's coordinated motion. To determine the number of eigenvectors that would represent the reduced subspace, we generated a scree plot of the eigenvalues

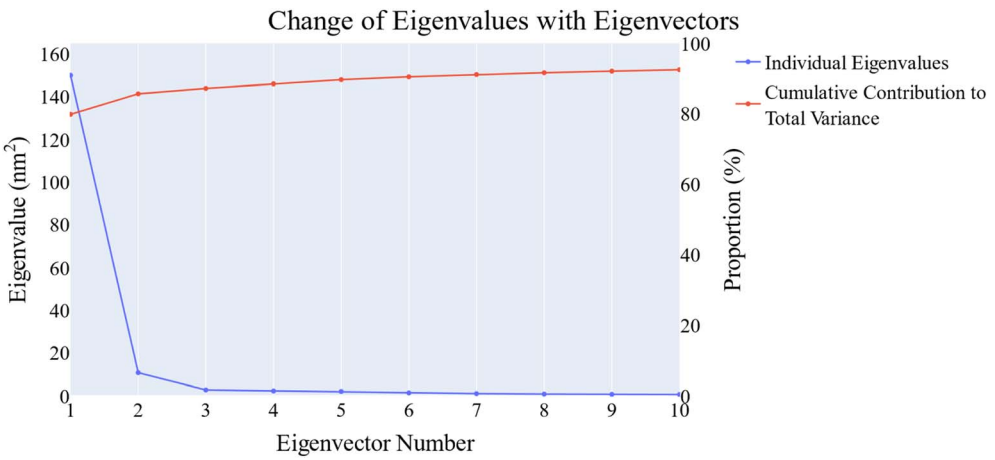

Fig. 14 The change in the eigenvalues with increasing the eigenvectors (blue line). In addition, the cumulative variance retained in the eigenvectors is shown (red line).

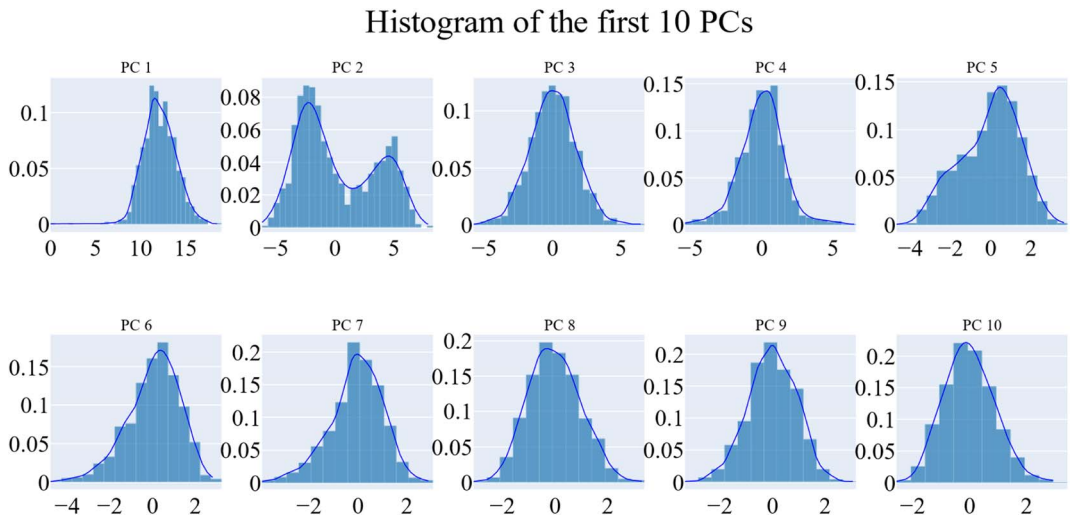

Fig. 15 The distribution of the first ten eigenvectors.

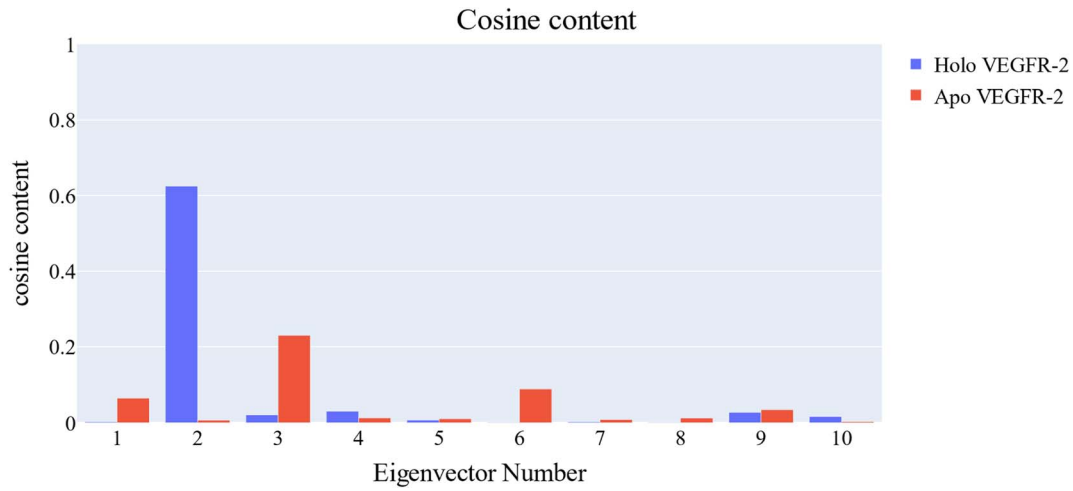

Fig. 16 Cosine content of the first ten eigenvectors for the two trajectories.

vs. the eigenvector index and found that the slope of the line connecting the points dramatically reduced at the second PC. We found that the first eigenvector alone accounted for 79.89% of the total variance and that the first three eigenvectors accounted for around 87.23% of the entire variance when added together (Fig. 14). In addition, the distribution of the first two eigenvectors was observed to be not Gaussian, while the distribution of the subsequent eigenvectors is (Fig. 15).

Cosine content was determined for both apo and holo VEGFR-2 simulations to determine the randomness of the motion captured by the first 10 eigenvectors. Except for the second eigenvector of the holo protein, which reaches up to 0.62, the first ten eigenvectors of the apo and holo proteins have cosine content values below 0.3 (Fig. 16). Therefore, the top three eigenvectors were used to represent the essential subspace. The root mean square inner product (RMSIP) shows that the two trajectories were sampled differently since there is only a 26.7% overlap between the two subspaces (the first three eigenvectors). In a similar vein, the RMSIP between the apo and holo C matrices only revealed a 36% resemblance.

3.3.6. Bidimensional projection studies. Fig. 17–19 show the results of projecting each trajectory onto the first three eigenvectors of the combined C matrix, with a bigger marker reflecting the average structure of each trajectory. Fig. 17 (projection on the first two eigenvectors) shows that the average structure differs significantly from the two trajectories with different sampling. As can be seen, the frames of the holo trajectory (red points) are clustered together compared to the apo trajectory frames (small blue points). Fig. 18 depicts the projection on the first and third eigenvectors, which shows that the two average structures are nearly the same and have a significantly larger overlap. Finally, projection on the second and third eigenvectors reveals that the two trajectories rarely intersect and that there is a significant discrepancy between the average structures. In addition, the holo trajectory appears to be clustered compared to the apo trajectory (Fig. 19). The motion

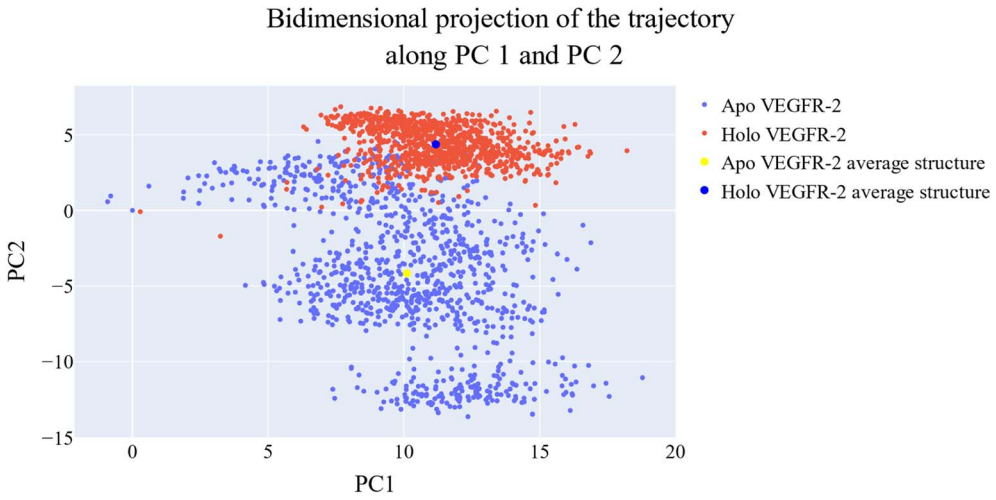

Fig. 17 Projection of each trajectory on the first two eigenvectors.

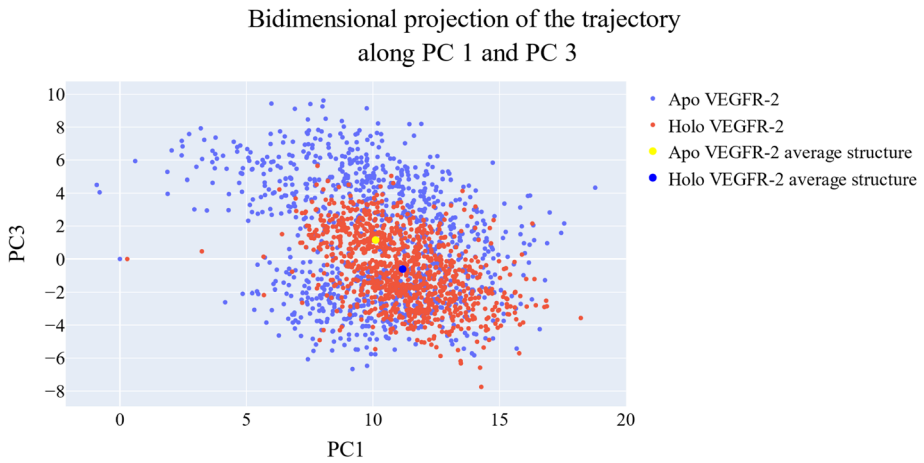

Fig. 18 Projection of each trajectory on the first and third eigenvectors.

represented by the first three eigenvectors was shown using porcupine diagrams (Fig. 20). More specifically, the Gly1046:-Leu1065 loop is the biggest motion represented by these three eigenvectors. In the case of the first eigenvector, both trajectories have the same motion captured (loop opening), but in different directions. The second eigenvector shows that in the

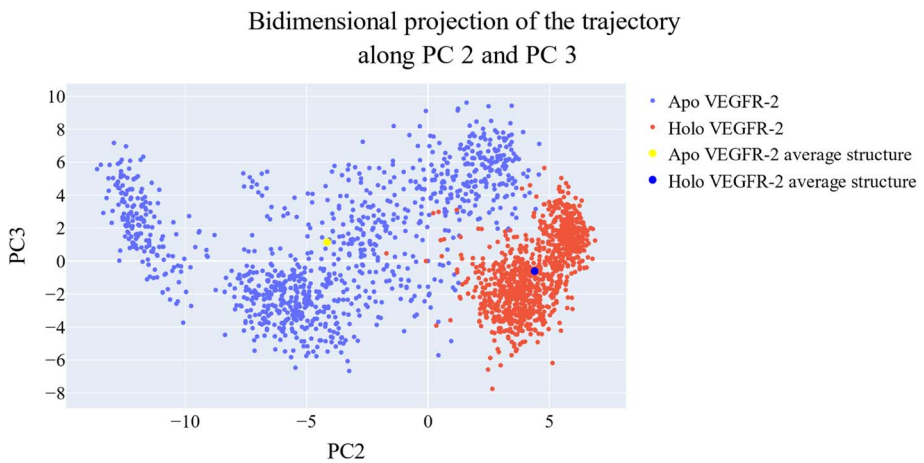

Fig. 19 Projection of each trajectory on the second and third eigenvectors.

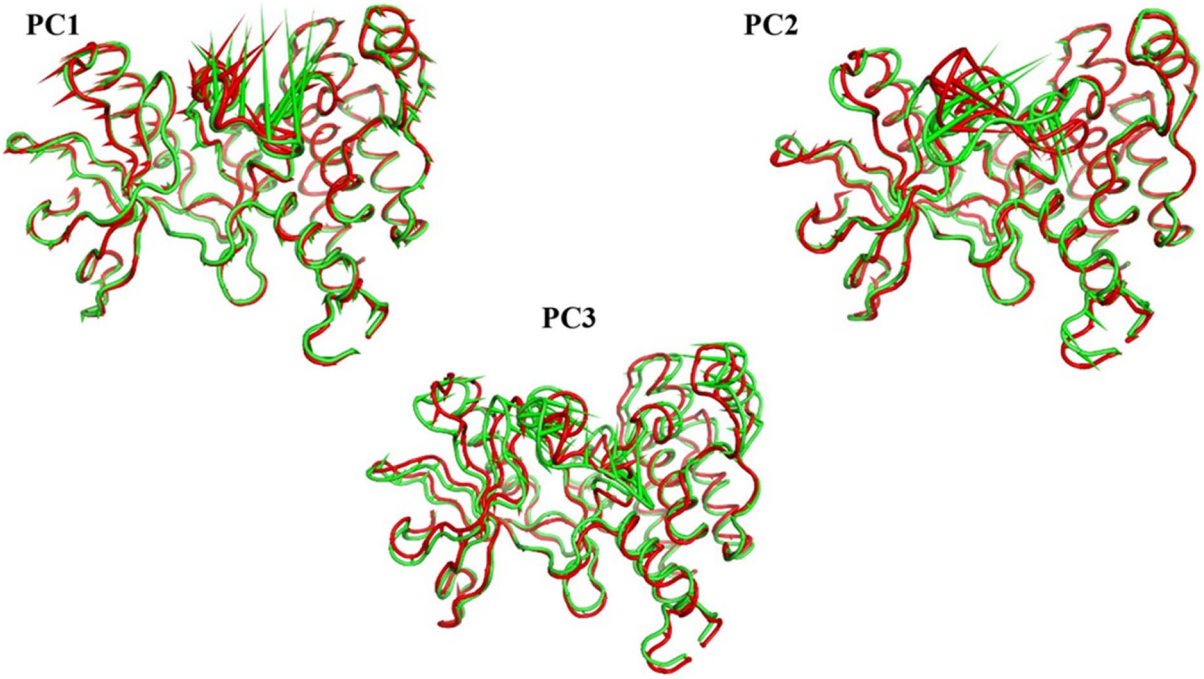

Fig. 20 Porcupine figures of each of the first three eigenvectors for both systems. Green cartoon: apo protein trajectory, red cartoon: holo protein trajectory.

apo structure (green), the loop opens, whereas, in the holo structure, it slightly closes (red). For both the apo and holo proteins, the third eigenvector indicates the loop's opening.

3.3.6. DFT calculations. DFT calculations are beneficial to optimize the chemical geometry and then determine the charge distribution role to design and improve potential inhibitor drugs. Additionally, DFT studies are beneficial to predict the binding mode with the target. After optimization using B3LYP functional and 6-311++G (d, p) basis set, the geometry of compound **15** in Fig. 21a, which is singlet, recorded a calculated dipole moment (D_m) of 5.04 Debye indicating reactive drug with high internal interactions. The chemical system of 56 atoms and 270 electrons shows effective charge transfer as depicted in the Mulliken charge analysis, Fig. 21b. All oxygen and N21 are negative but C30 and C32 are the most negative atoms. Both N25 and N26 are positive while N21 is negative due to the resonance within the drug structure. C31 and C19 are the most positive atoms in the proposed compound which qualified to play as targets of nucleophilic assault.

The frontiers molecular orbitals HOMO and LUMO provide insight into the molecular reactivity and then give information about physical and structural features of the molecular system. In addition, the molecule's excitation energy between HOMO and LUMO is a parameter that determines the possible transition within the molecule suggesting a biologically reactive or nonreactive molecule. Both HOMO and LUMO electronic lobes are concentrated over the thiazolidine half of compound **15** as demonstrated in Fig. 21c and associated with an energy gap, E_{gap} of 3.77 eV which is a reasonable value enabling the electronic transition easily within compound **15**. Also, the E_{gap} illustrates how the structure's internal charge will ultimately transfer.[77] The global reactivity parameters associated with HOMO and LUMO energies were calculated and listed in Table 8. All calculated parameters revealed that the chemical system of compound **15** is soft and reactive.

It is an essential principle of chemistry that electrons and nuclei attract one another whereas electrons repel one another. These electrostatic forces simply balance in a molecule's equilibrium geometry. The force acting on a nucleus in a molecular system is equal to the total of the coulombic forces generated by the other nuclei and the distribution of electrons, according to the fundamentally significant Hellman–Feynman theorem. The electrostatic potential: ESP, surface is produced using Gaussian software based on these computations and techniques. The surface diagram of the molecular electrostatic potential that depicts the distribution of the electronic charge is provided in Fig. 21d. It is apparent that compound **15** had a balanced charge distribution, making it sticky to a variety of biological targets.[78] The total density of states (TDOS) was analyzed using GaussSum to explore the place of maximum density. Fig. 21e shows the TDOS spectrum of compound **15**, and the results conducted that the total density is not focused on the HOMO orbital, but it is localized over orbitals under HOMO.

The quantum theory of atoms in molecules (QTAIM) technique is studied using Multiwfn and ALIMAll programs based on topological analysis. The results are briefly demonstrated in Fig. 21f and g while the detailed analysis and calculated parameters are presented in Fig. S1 and Table S1 in the ESI file.†

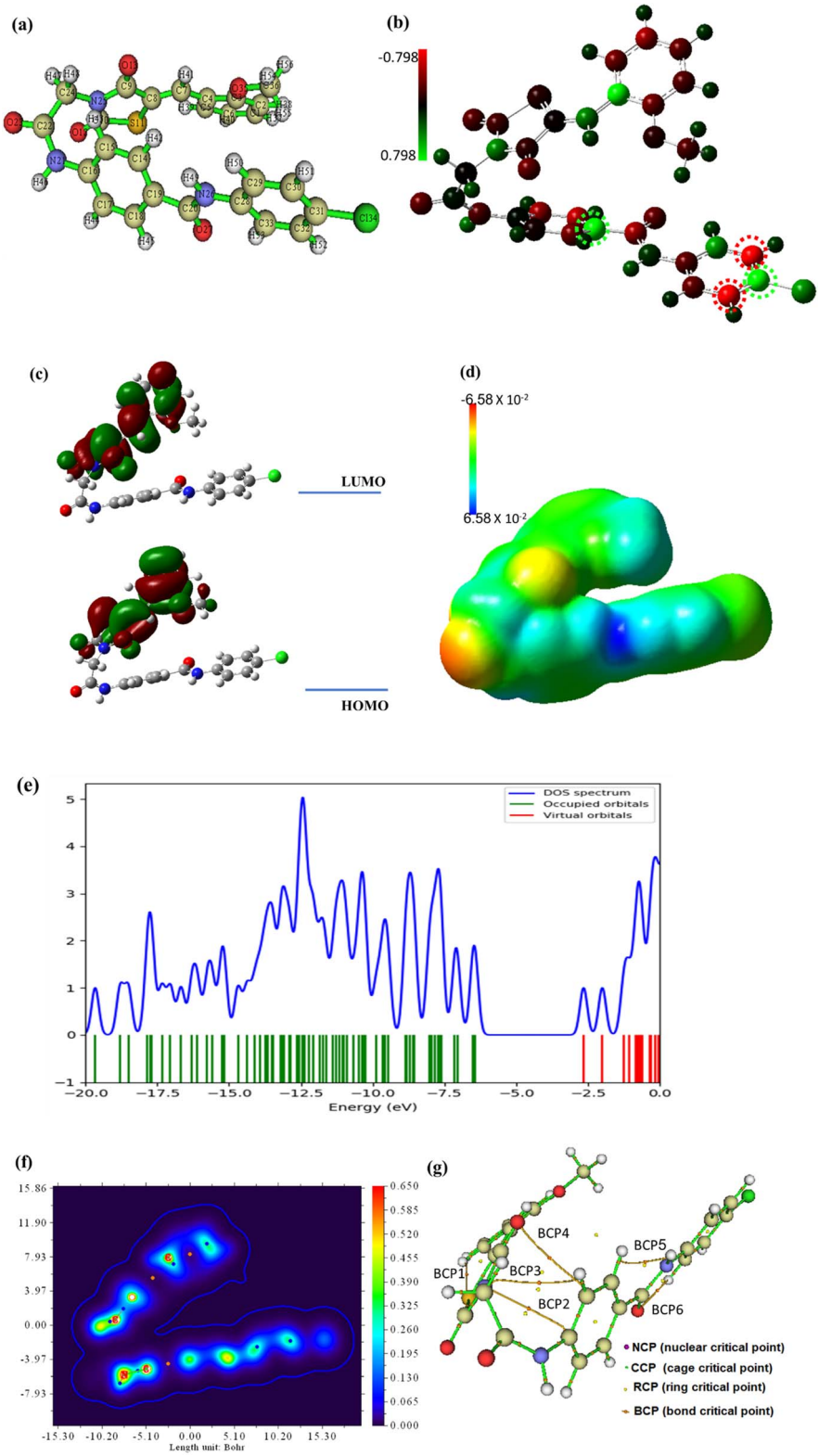

Fig. 21 The optimized geometry (a), the Mullikan atomic charge distribution (b), the frontier molecular orbitals (c), the electrostatic potential (d), the total density of states (e), and the QTAIM maps (f and g) at B3LYB/6-311+G(d,p) for compound **15**.

Based on the values of the electron density, (ρ), the results show that compound **15** is two folded (Fig. 21f) and new bond paths have been developed as shown in Fig. 21g and S1.† According to the Laplacian values, ($\nabla^2\rho$) and energy density, $H(r)$, values in Table 1S† compound **15** is stable as the most significant BCPs are noncovalent or closed bonding.

Table 8 The DFT calculated global reactivity parameters for compound **15**

IP	EA	μ (eV)	χ (eV)	η (eV)	σ (eV)	ω (eV)	D_m (Debye)	TE (eV)	ΔN_{max}	ΔE (eV)
6.421	2.648	−4.535	4.535	1.886	0.530	19.390	5.041	−65364.3	2.404	−19.390

Table 9 ADMET screening of the derivatives **12–17**

Comp.	BBB level	Solubility level	Absorption level	CYP2D6 prediction	PPB prediction
12	Very low	Low	Good	Non-inhibitor	>90%
13					
14		Very low	Moderate		
15		Low			
16					<90%
17			Poor		
Sorafenib		Very low	Good		>90%

3.3.7. *In silico* ADMET analysis. Nearly 50% of new medication candidates are thought to fail due to unsatisfactory efficacy,[79] while up to 40% of drug candidates have previously failed due to toxicity.[80] Drugs including soruvidine, phenylpropanolamine hydrochloride, and mibefradil have been taken off the market because of toxicity or drug–drug interactions.[81] Both regulators and drug manufacturers now recognize that ADMET investigations, in addition to pharmacological qualities, are essential to a drug candidate's success. These investigations are now conducted early in the drug discovery process because of their influence on future success.

In silico ADMET studies of the synthesized compounds as the reference molecule sorafenib were carried out using Discovery Studio software. The results were illustrated in Table 9 and Fig. 22.

The results revealed that the synthesized compounds have very low BBB penetration powers. So that, it can be detected that CNS adverse effects are absent upon ingestion of these compounds. Although the results clarified that the synthesized compounds have low to very low aqueous solubility, compounds **12** and **13** were expected to have good levels of absorption. Also, compounds **14**, **15**, and **16** were predicted to have moderate absorption levels. Moreover, all the synthesized compounds were predicted to possess non-inhibitory potential against the

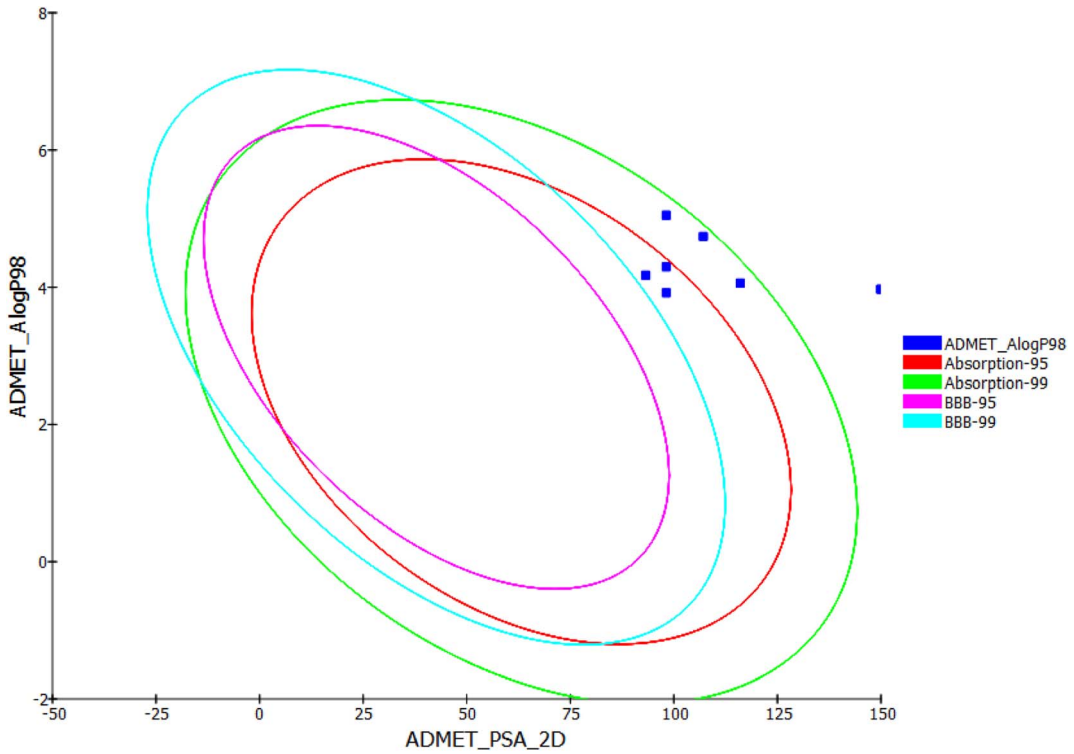

Fig. 22 ADMET profile of the derivatives **12–17**.

Table 10 Toxicity study of the derivatives 12–17

Comp.	Ames prediction	Mouse-female FDA	Carcinogenic potency TD_{50}[a] (Mouse)	Rat oral LD_{50}[b]	Rat chronic LOAEL[b]	Skin irritancy	Ocular irritancy
12	Non-mutagen	Non-carcinogen	26.143	1.144	0.037	Non-irritant	Mild
13			20.270	0.933	0.012		
14			14.274	2.835	0.017		
15			24.219	1.627	0.008		
16			29.495	3.031	0.011		
17			37.391	1.498	0.010		
Sorafenib		Single-carcinogen	19.236	0.823	0.005		

[a] Unit: mg kg^{-1} body weight/day. [b] Unit: g kg^{-1} body weight.

CYP2D6. Finally, compounds **12**, **13**, **14**, and **15** were predicted to bind plasma protein with levels more than 90%, while compounds **16** and **17** were expected to bind plasma protein with less than 90%.

3.3.8. Toxicity studies. To calculate the expected toxicity potential of the synthesized compounds, seven toxicity models were investigated using Discovery Studio software[82,83] and sorafenib as a reference compound. The results were presented in Table 10 and ESI.†

The Ames prediction and FDA rodent carcinogenicity models revealed that all the synthesized compounds are non-mutagenic and non-carcinogenic.

The tested molecules showed calculated carcinogenic potency TD_{50} values ranging from 14.274 to 29.495 mg kg^{-1} day^{-1}, which were higher than that of sorafenib (19.236 mg kg^{-1} day^{-1}, respectively). In addition, all the synthesized compounds were expected to have oral LD_{50} values ranging from 0.933 to 3.031 g kg^{-1}, which were more than that of sorafenib (0.823 g kg^{-1}). Furthermore, the calculated LOAEL values of the synthesized compounds ranged from 0.008 to 0.037 g kg^{-1}, which were higher than that of sorafenib (0.005 g kg^{-1}). Finally, the synthesized compounds were predicted to be non-irritant for the skin and mild irritant for the eye.

3.4. Correlation of *in silico* studies and biological results

The reference molecule in biological and docking studies is sorafenib. In molecular docking, sorafenib participated in five hydrogen-bonding interactions. Specifically, two hydrogen bonds formed between the picolinamide group of sorafenib and Cys917 at the hinge region, while three hydrogen bonds were

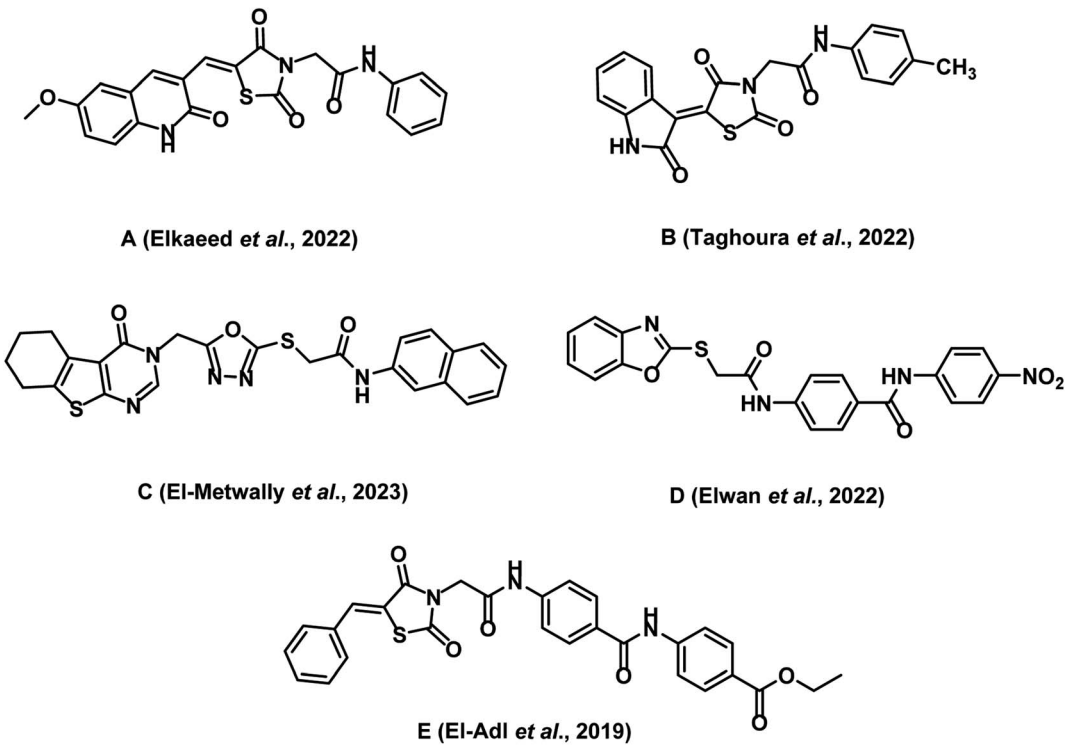

Fig. 23 Reported VEGFR-2 inhibitors by our research group. (A) 2-Oxo-1,2-dihydroquinoline derivative. (B) 2-Oxoindoline derivative. (C) Thieno[2,3-*d*]pyrimidine derivative. (D) Benzo[*d*]oxazole derivative. (E) Thiazolidine-2,4-dione derivative.

established between the urea moiety of sorafenib and ASP1044 and Glu883 at the DFG motif region. Similarly, compound **15** established three hydrogen bonds with Cys917, Asp1044, and Glu883. Furthermore, owing to the significant number of hydrophobic and van der Waals interactions between compound **15** and the active site, compound **15** exhibited a higher binding energy compared to Sorafenib. The resemblance in binding modes between compound **15** ($\Delta G = -24.62$ kcal mol^{-1}) and sorafenib ($\Delta G = -21.33$ kcal mol^{-1}) elucidates the closely related VEGFR-2 inhibitory activities of both compound **15** ($IC_{50} = 0.081$ μM) and sorafenib ($IC_{50} = 0.061$ μM).

Compounds **12** and **17** exhibited moderate VEGFR-2 inhibitory activities, displaying IC_{50} values of 0.477 and 0.976 μM, respectively. Similarly, compounds **13**, **14**, and **16** displayed weak VEGFR-2 inhibitory activities, with IC_{50} values of 0.157, 1.586, and 1.152 μM, respectively. Notably, these compounds adopted a binding mode resembling that of the reference sorafenib. The reduction in the VEGFR-2 inhibitory activities of these compounds despite their binding similarity to sorafenib, could potentially be attributed to a decrease in their solubility. As indicated by ADMET studies, compounds **12**, **13**, **14**, **16**, and **17** exhibit low to very low solubility levels. Consequently, it becomes crucial to make modifications to these lead compounds in order to produce derivatives with improved water solubility. In contrast, the synthesized compounds were projected to fall within an acceptable range of toxicity potential against the tested models.

A comparative study between the activity of the newly synthesized compounds and the previously identified lead molecules by our research group has yielded valuable insights into the drug discovery process. For this analysis, we focused on five active lead compounds (designated as **A**, **B**, **C**, **D**, and **E**) that were previously reported by our team. These compounds exhibit a high degree of structural similarity, with variations in functional groups while preserving the crucial pharmacophoric features required for VEGFR-2 inhibition (Fig. 23).[15,21,35,84,85]

Regarding VEGFR-2 inhibitory activity, compound **15** ($IC_{50} = 0.081$ μM) showed higher activity than compound **A** ($IC_{50} = 0.137$ μM), compound **B** ($IC_{50} = 0.116$ μM), compound **C** ($IC_{50} = 0.580$ μM), and compound **E** ($IC_{50} = 0.22$ μM). In contrast, compound **15** showed a lower activity than the reported benzoxazole lead compound **D** ($IC_{50} = 0.055$ μM). This deviation in activity may be related the favorable impact of benzoxazole as an anticancer nucleus.

For selectivity indices against tumor cell lines, compound **15** showed selectivity indices of 28.73, 21.89, and 28.15 against HT-29, A549, and HCT-116, respectively. These values surpassed the reported selectivity index values for compound **A**.

Regarding the activity of compound **15** against BAX, Bcl-2, caspases-8, and caspases −9, it was more promising than compound **C**. Specifically, compound **15** displayed heightened effects against BAX, Bcl-2, and caspase-9 compared to compound **C**. However, compound **C** demonstrated a stronger effect against caspase-8 compared to compound **15**. Concerning the activity of compound **15** against TNF-α and IL6, it showed comparable effect to compound **C** against TNF-α. On the other hand, it showed higher inhibitory activity against IL-6 than compound **C**.

4. Conclusion

In conclusion, this study successfully designed and synthesized novel VEGFR-2-targeting thiazolidine-2,4-dione derivatives with promising anticancer properties. Compound **15** emerged as the most potent inhibitor of VEGFR-2, displaying an IC_{50} value of 0.081 μM. It also exhibited significant anti-proliferative activities against three different cancer cell lines (HT-29, A-549, and HCT-116), with IC_{50} values ranging from 13.56 to 17.8 μM. SAR study revealed that the substitution of the terminal phenyl ring with electron withdrawing group (Cl and NO_2) is more advantageous than the substitution with electron donating group (OCH_3). In addition, the hydrophobic group (Cl) is more helpful than the hydrophilic group (NO_2) as substituents on hydrophobic tail. Also, the planarity of hydrophobic tail (sp2 hybridization) is more valuable than the non-planarity (sp^3 hybridization). Furthermore, compound **15** demonstrated a great ability to induce apoptosis in HT-29 cancer cells and induce cell cycle arrest in the S phase. Mechanistically, it upregulated BAX and downregulated Bcl-2, while also increasing the levels of caspase-8 and caspase-9. Computational analysis of the VEGFR-2-**15** complex using molecular docking, molecular dynamics simulations and essential dynamics provided insights into its kinetic and structural characteristics. The study also assessed the drug likeness potential of the designed molecules through computational ADMET and toxicity tests. Overall, these findings highlight compound **15** as a potent anticancer agent and provide valuable guidance for future endeavors in the development of novel anticancer therapeutics.

Conflicts of interest

There are no conflicts of interest to declare.

Acknowledgements

This research was funded by Princess Nourah bint Abdulrahman University Researchers Supporting Project number (PNURSP2023R142), Princess Nourah bint Abdulrahman University, Riyadh, Saudi Arabia. The authors extend their appreciation to the Research Center at AlMaarefa University for funding this work.

References

1 F. Biemar and M. Foti, *Cancer Biol. Med.*, 2013, **10**, 183.
2 R. A. Ward, S. Fawell, N. Floc'h, V. Flemington, D. McKerrecher and P. D. Smith, *Chem. Rev.*, 2020, **121**, 3297–3351.
3 A. Belal, N. M. Abdel Gawad, A. B. Mehany, M. A. Abourehab, H. Elkady, A. A. Al-Karmalawy and A. S. Ismael, *J. Enzyme Inhib. Med. Chem.*, 2022, **37**, 1884–1902.
4 W. M. Eldehna, M. A. El Hassab, Z. M. Elsayed, T. Al-Warhi, H. Elkady, M. F. Abo-Ashour, M. A. Abourehab, I. H. Eissa and H. A. Abdel-Aziz, *Sci. Rep.*, 2022, **12**, 12821.

5 R. Trenker and N. Jura, *Curr. Opin. Cell Biol.*, 2020, **63**, 174–185.
6 X. Wang, A. M. Bove, G. Simone and B. Ma, *Front. Cell Dev. Biol.*, 2020, **8**, 599281.
7 S. J. Modi and V. M. Kulkarni, *Med. Drug Discov*, 2019, **2**, 100009.
8 S. R. Silva, K. A. Bowen, P. G. Rychahou, L. N. Jackson, H. L. Weiss, E. Y. Lee, C. M. Townsend Jr and B. M. Evers, *Int. J. Cancer*, 2011, **128**, 1045–1056.
9 N. Nishida, H. Yano, T. Nishida, T. Kamura and M. Kojiro, *Vasc. Health Risk Manag.*, 2006, **2**, 213–219.
10 K. McCardle and J. Pan, *Nat. Comput. Sci.*, 2022, **2**, 134–136.
11 T. Engel, *J. Chem. Inf. Model.*, 2006, **46**, 2267–2277.
12 J. Xu and A. Hagler, *Molecules*, 2002, **7**, 566–600.
13 E. B. Elkaeed, R. G. Yousef, H. Elkady, I. M. Gobaara, B. A. Alsfouk, D. Z. Husein, I. M. Ibrahim, A. M. Metwaly and I. H. Eissa, *Molecules*, 2022, **27**, 4606.
14 R. G. Yousef, A. Elwan, I. M. Gobaara, A. B. Mehany, W. M. Eldehna, S. A. El-Metwally, B. A. Alsfouk, E. B. Elkaeed, A. M. Metwaly and I. H. Eissa, *J. Enzyme Inhib. Med. Chem.*, 2022, **37**, 2206–2222.
15 M. S. Taghour, H. Elkady, W. M. Eldehna, N. M. El-Deeb, A. M. Kenawy, E. B. Elkaeed, A. A. Alsfouk, M. S. Alesawy, A. M. Metwaly and I. H. Eissa, *J. Enzyme Inhib. Med. Chem.*, 2022, **37**, 1903–1917.
16 M. S. Taghour, H. Elkady, W. M. Eldehna, N. El-Deeb, A. M. Kenawy, E. B. Elkaeed, B. A. Alsfouk, M. S. Alesawy, D. Z. Husein and A. M. Metwaly, *PLoS One*, 2022, **17**, e0272362.
17 E. B. Elkaeed, R. G. Yousef, H. Elkady, I. M. Gobaara, A. A. Alsfouk, D. Z. Husein, I. M. Ibrahim, A. M. Metwaly and I. H. Eissa, *Processes*, 2022, **10**, 1391.
18 R. G. Yousef, H. Elkady, E. B. Elkaeed, I. M. Gobaara, H. A. Al-Ghulikah, D. Z. Husein, I. M. Ibrahim, A. M. Metwaly and I. H. Eissa, *Molecules*, 2022, **27**, 7719.
19 M. S. Taghour, H. Elkady, W. M. Eldehna, N. El-Deeb, A. M. Kenawy, A. E. Abd El-Wahab, E. B. Elkaeed, B. A. Alsfouk, A. M. Metwaly and I. H. Eissa, *J. Biomol. Struct. Dyn.*, 2022, 1–16.
20 E. B. Elkaeed, R. G. Yousef, H. Elkady, I. M. Gobaara, A. A. Alsfouk, D. Z. Husein, I. M. Ibrahim, A. M. Metwaly and I. H. Eissa, *Processes*, 2022, **10**, 1391.
21 E. B. Elkaeed, M. S. Taghour, H. A. Mahdy, W. M. Eldehna, N. M. El-Deeb, A. M. Kenawy, B. A. Alsfouk, M. A. Dahab, A. M. Metwaly and I. H. Eissa, *J. Enzyme Inhib. Med. Chem.*, 2022, **37**, 2191–2205.
22 K. Lee, K.-W. Jeong, Y. Lee, J. Y. Song, M. S. Kim, G. S. Lee and Y. Kim, *Eur. J. Med. Chem.*, 2010, **45**, 5420–5427.
23 V. A. Machado, D. Peixoto, R. Costa, H. J. Froufe, R. C. Calhelha, R. M. Abreu, I. C. Ferreira, R. Soares and M.-J. R. Queiroz, *Bioorg. Med. Chem.*, 2015, **23**, 6497–6509.
24 Z. Wang, N. Wang, S. Han, D. Wang, S. Mo, L. Yu, H. Huang, K. Tsui, J. Shen and J. Chen, *PLoS One*, 2013, **8**, e68566.
25 J. Dietrich, C. Hulme and L. H. Hurley, *Bioorg. Med. Chem.*, 2010, **18**, 5738–5748.
26 Q.-Q. Xie, H.-Z. Xie, J.-X. Ren, L.-L. Li and S.-Y. Yang, *J. Mol. Graph. Model.*, 2009, **27**, 751–758.
27 R. N. Eskander and K. S. Tewari, *Gynecol. Oncol.*, 2014, **132**, 496–505.
28 S. Wilhelm, C. Carter, M. Lynch, T. Lowinger, J. Dumas, R. A. Smith, B. Schwartz, R. Simantov and S. Kelley, *Nat. Rev. Drug Discov.*, 2006, **5**, 835–844.
29 S. M. Wilhelm, J. Dumas, L. Adnane, M. Lynch, C. A. Carter, G. Schütz, K. H. Thierauch and D. Zopf, *Int. J. Cancer*, 2011, **129**, 245–255.
30 R. Roskoski, *Biochem. Biophys. Res. Commun.*, 2007, **356**, 323–328.
31 G. J. Roth, R. Binder, F. Colbatzky, C. Dallinger, R. Schlenker-Herceg, F. Hilberg, S.-L. Wollin and R. Kaiser, *J. Med. Chem.*, 2015, **58**, 1053–1063.
32 L. J. Scott, *Drugs*, 2015, **75**, 553–560.
33 P. Norman, *Expert Opinion on Orphan Drugs*, 2015, **3**, 445–455.
34 R. Elisei, M. J. Schlumberger, S. P. Müller, P. Schöffski, M. S. Brose, M. H. Shah, L. Licitra, B. Jarzab, V. Medvedev and M. C. Kreissl, *J. Clin. Oncol.*, 2013, **31**, 3639.
35 A. Elwan, A. E. Abdallah, H. A. Mahdy, M. A. Dahab, M. S. Taghour, E. B. Elkaeed, A. B. Mehany, A. Nabeeh, M. Adel and A. A. Alsfouk, *Molecules*, 2022, **27**, 5047.
36 H. A. Mahdy, M. K. Ibrahim, A. M. Metwaly, A. Belal, A. B. Mehany, K. M. El-Gamal, A. El-Sharkawy, M. A. Elhendawy, M. M. Radwan and M. A. Elsohly, *Bioorg. Chem.*, 2020, **94**, 103422.
37 M. M. Alanazi, I. H. Eissa, N. A. Alsaif, A. J. Obaidullah, W. A. Alanazi, A. F. Alasmari, H. Albassam, H. Elkady and A. Elwan, *J. Enzyme Inhib. Med. Chem.*, 2021, **36**, 1760–1782.
38 I. H. Eissa, R. El-Haggar, M. A. Dahab, M. F. Ahmed, H. A. Mahdy, R. I. Alsantali, A. Elwan, N. Masurier and S. S. Fatahala, *J. Enzyme Inhib. Med. Chem.*, 2022, **37**, 1587–1599.
39 N. A. Alsaif, M. S. Taghour, M. M. Alanazi, A. J. Obaidullah, W. A. Alanazi, A. Alasmari, H. Albassam, M. A. Dahab and H. A. Mahdy, *Bioorg. Med. Chem.*, 2021, **46**, 116384.
40 N. A. Alsaif, H. A. Mahdy, M. M. Alanazi, A. J. Obaidullah, H. M. Alkahtani, A. M. Al-Hossaini, A. A. Al-Mehizi, A. Elwan and M. S. Taghour, *Arch. Pharmazie*, 2022, **355**, 2100359.
41 T. Slater, B. Sawyer and U. Sträuli, *Biochim. Biophys. Acta*, 1963, **77**, 383–393.
42 A. Van de Loosdrecht, R. Beelen, g. Ossenkoppele, M. Broekhoven and M. J. Langenhuijsen, *J. Immunol. Methods*, 1994, **174**, 311–320.
43 M. C. Alley, D. A. Scudiero, A. Monks, M. L. Hursey, M. J. Czerwinski, D. L. Fine, B. J. Abbott, J. G. Mayo, R. H. Shoemaker and M. R. Boyd, *Cancer Res.*, 1988, **48**, 589–601.
44 E. B. Elkaeed, R. G. Yousef, H. Elkady, A. B. Mehany, B. A. Alsfouk, D. Z. Husein, I. M. Ibrahim, A. M. Metwaly and I. H. Eissa, *J. Biomol. Struct. Dyn.*, 2022, 1–16.
45 H. Raza, A. John, E. M. Brown, S. Benedict and A. Kambal, *Toxicol. Appl. Pharmacol.*, 2008, **226**, 161–168.
46 H. Raza, A. John and S. Benedict, *Eur. J. Pharmacol.*, 2011, **668**, 15–24.

47 X.-D. Yu, J.-l. Yang, W.-L. Zhang and D.-X. Liu, *Tumor Biol.*, 2016, **37**, 2871–2877.
48 A. Balah, O. Ezzat and E.-S. Akool, *Int. Immunopharm.*, 2018, **65**, 493–502.
49 N. M. Aborehab, M. R. Elnagar and N. E. Waly, *J. Biochem. Mol. Toxicol.*, 2020, e22638.
50 M. R. Elnagar, A. B. Walls, G. K. Helal, F. M. Hamada, M. S. Thomsen and A. A. Jensen, *Eur. J. Pharmacol.*, 2018, **826**, 106–113.
51 Y. Guo, Y. Tong, H. Zhu, Y. Xiao, H. Guo, L. Shang, W. Zheng, S. Ma, X. Liu and Y. Bai, *Cell Biol. Toxicol.*, 2021, **37**, 479–496.
52 C. Jiao, W. Chen, X. Tan, H. Liang, J. Li, H. Yun, C. He, J. Chen, X. Ma and Y. Xie, *J. Ethnopharmacol.*, 2020, **247**, 112256.
53 M. M. Alanazi, H. Elkady, N. A. Alsaif, A. J. Obaidullah, H. M. Alkahtani, M. M. Alanazi, M. A. Alharbi, I. H. Eissa and M. A. Dahab, *RSC Adv.*, 2021, **11**, 30315–30328.
54 E. B. Elkaeed, I. H. Eissa, H. Elkady, A. Abdelalim, A. M. Alqaisi, A. A. Alsfouk, A. Elwan and A. M. Metwaly, *Int. J. Mol. Sci.*, 2022, **23**, 8407.
55 E. B. Elkaeed, H. Elkady, A. Belal, B. A. Alsfouk, T. H. Ibrahim, M. Abdelmoaty, R. K. Arafa, A. M. Metwaly and I. H. Eissa, *Processes*, 2022, **10**, 530.
56 M. J. Abraham, T. Murtola, R. Schulz, S. Páll, J. C. Smith, B. Hess and E. Lindahl, *SoftwareX*, 2015, **1**, 19–25.
57 E. B. Elkaeed, F. S. Youssef, I. H. Eissa, H. Elkady, A. A. Alsfouk, M. L. Ashour, M. A. El Hassab, S. M. Abou-Seri and A. M. Metwaly, *Int. J. Mol. Sci.*, 2022, **23**, 6912.
58 S. Jo, X. Cheng, S. M. Islam, L. Huang, H. Rui, A. Zhu, H. S. Lee, Y. Qi, W. Han and K. Vanommeslaeghe, *Adv. Protein Chem. Struct. Biol.*, 2014, **96**, 235–265.
59 E. B. Elkaeed, B. A. Alsfouk, T. H. Ibrahim, R. K. Arafa, H. Elkady, I. M. Ibrahim, I. H. Eissa and A. M. Metwaly, *Antivir. Ther.*, 2023, **28**, 13596535231199838.
60 T. J. Tuccinardi, *Expet Opin. Drug Discov.*, 2021, **16**, 1233–1237.
61 M. S. Valdés-Tresanco, M. E. Valdés-Tresanco, P. A. Valiente and E. J. Moreno, *J. Chem. Theor. Comput.*, 2021, **17**, 6281–6291.
62 C. Bouysset and S. Fiorucci, *J. Cheminf.*, 2021, **13**, 1–9.
63 S. Salentin, S. Schreiber, V. J. Haupt, M. F. Adasme and M. Schroeder, *Nucleic Acids Res.*, 2015, **43**, W443–W447.
64 T. Tubiana, J.-C. Carvaillo, Y. Boulard and S. Bressanelli, *J. Chem. Inf. Model.*, 2018, **58**, 2178–2182.
65 A. Amadei, A. B. Linssen and H. J. Berendsen, *Proteins: Struct., Funct., Bioinf.*, 1993, **17**, 412–425.
66 E. Papaleo, P. Mereghetti, P. Fantucci, R. Grandori and L. De Gioia, *J. Mol. Graph. Model.*, 2009, **27**, 889–899.
67 G. G. Maisuradze and D. M. Leitner, *Proteins: Struct., Funct., Bioinf.*, 2007, **67**, 569–578.
68 B. Hess, *Phys. Rev. E*, 2000, **62**, 8438.
69 K. Kar, U. Krithika, P. Basu, S. S. Kumar, A. Reji and B. P. Kumar, *Bioorg. Chem.*, 2014, **56**, 27–33.
70 J. Biradar and B. Sasidhar, *Eur. J. Med. Chem.*, 2011, **46**, 6112–6118.
71 V. Gududuru, E. Hurh, J. T. Dalton and D. D. Miller, *Bioorg. Med. Chem. Lett*, 2004, **14**, 5289–5293.
72 E. Shacter and S. Weitzman, *J. Oncol.*, 2002, **16**, 217–226, 229; discussion 230.
73 L. S. Angelo and R. Kurzrock, *Clin Cancer Res.*, 2007, **13**, 2825–2830.
74 Y. Zhang, X. Ding, C. Miao and J. Chen, *BMC Anesthesiol.*, 2019, **19**, 1–11.
75 X.-M. Ou, W.-C. Li, D.-S. Liu, Y.-P. Li, F.-Q. Wen, Y.-L. Feng, S.-F. Zhang, X.-Y. Huang, T. Wang and K. Wang, *Int. Immunopharm.*, 2009, **9**, 70–79.
76 S. Tian, H. Quan, C. Xie, H. Guo, F. Lü, Y. Xu, J. Li and L. Lou, *Cancer Sci.*, 2011, **102**, 1374–1380.
77 D. Z. Husein, R. Hassanien and M. Khamis, *RSC Adv.*, 2021, **11**, 27027–27041.
78 T. Wang and D. Z. Husein, *Environ. Sci. Pollut. Res.*, 2023, **30**, 8928–8955.
79 T. Kennedy, *Drug discovery today*, 1997, **2**, 436–444.
80 J. A. DiMasi, *Clin. Pharmacol. Ther.*, 1995, **58**, 1–14.
81 A. P. Li, *Drug discovery today*, 2001, **6**, 357–366.
82 X. Xia, E. G. Maliski, P. Gallant and D. Rogers, *J. Med. Chem.*, 2004, **47**, 4463–4470.
83 *BIOVIA, QSAR., ADMET and Predictive Toxicology*, **https://www.3dsbiovia.com/products/collaborative-science/biovia-discovery-studio/qsar-admet-and-predictive-toxicology.html**, accessed May 2020.
84 S. A. El-Metwally, A. A. Abuelkhir, H. Elkady, M. S. Taghour, I. M. Ibrahim, D. Z. Husein, A. A. Alsfouk, A. Sultan, A. Ismail and S. Y. Elkhawaga, *Comput. Biol. Chem.*, 2023, 107928.
85 K. El-Adl, A.-G. A. El-Helby, H. Sakr, I. H. Eissa, S. S. El-Hddad and F. M. Shoman, *Bioorg. Chem.*, 2020, **102**, 104059.